Structural Dynamics of 1T-$TiSe_2$ Using Femtosecond Electron Diffraction

by

Aminat Oyiza Suleiman

Thesis presented in partial fulfilment of the requirements
for the degree of

Master of Science

at Stellenbosch University

Department of Physics,
Stellenbosch University,
Private Bag X1, 7602 Matieland, South Africa.

Supervisors:

Prof Heinrich P. H. Schwoerer
Prof Erich G. Rohwer

December 2014

Declaration

By submitting this thesis electronically, I declare that the entirety of the work contained therein is my own, original work, that I am the sole author thereof (save to the extent explicitly otherwise stated), that reproduction and publication thereof by Stellenbosch University will not infringe any third party rights and that I have not previously in its entirety or in part submitted it for obtaining any qualification.

Date: November 2014 .....

Abstract

Trilayered transition metal dichalcogenides such as our sample ($1T$-$TiSe_2$) have been studied for many years as systems with strong electron-electron and electron-phonon correlations. The main attraction to this family of compound is its potential to exhibit ground state phenomena known as charge density waves whose detailed physical origin has been controversially determined.

In this study, we have used an ultrafast femtosecond laser based on a pump-probe technique, namely ultrafast electron diffraction, to investigate these exotic features associated with the crystal. A pump laser pulse photo-excites the crystal from its ground state and the probe pulse (ultrashort electron pulse) takes the snapshot of the evolution of the lattice generating an electron diffraction pattern of the crystal. Hence the dynamical structural behaviour can be observed in time with a subpicosecond temporal resolution. As a hexagonal close-packed structure, its signature is expected to be seen in the diffraction pattern in both a steady-state and electron time-resolved femtosecond electron diffraction.

In addition, simulations of electron diffractions pattern for room and low temperature structural data via a software called Simulation and Analysis of Electron diffraction (SAED) have been carried out. Clear signatures of charge density waves were seen at low temperature.

Opsomming

Drie-laag oorgangsmetaal dikhalkogeniedes soos ons voorbeeld (1T-$TiSe_2$), word reeds vir baie jare bestudeer as sisteme met sterk elektron-elektron en elektron-fonon korrelasies. Die hoof aantrekkingskrag van hierdie sisteme is die verskynsel van ladingdigtheidsgolwe in die grondtoestand. Die fisiese oorsprong van hierdie ladingdigtheidsgolwe was bepaal te midde van verskeie teenstrydighede.

In hierdie studie, maak ons gebruik van die ultravinnige femtosekonde laser gebaseerde aktiveer-interogeer tegniek, genaamd ultravinnige elektron diffraksie (UED) om unicke eienskappe wat met die kristal geassosieer is te bestudeer. In UED wek 'n ultravinnige laserpuls (aktivering) die kristal op vanaf die grondtoestand waartydens n ultravinnige elektronpuls (interogering) 'n foto neem van die evolusie van die elektron diffraksiepatroon wat deur die kristalrooster gegenereer word. Hierdie wisselwerking van die interogerings elektronpuls en die sisteem kan gevolglik teen verskeie vasgetelde tye toegelaat word. Dus kan die dinamiese strukturele gedrag waargeneem word met 'n tydresolusie in die orde van die elektronpuls (sub-pikosekondes). Siende dat die kristal 'n diggepakte-heksagonale struktuur vorm, behoort die kenmerkende diffraksiepatroon daarvan waarneembaar te wees in beide die bestendige diffraksie en femtosekonde elektron diffraksie tegnieke. In hierdie konteks was duidelike tekens van ladingdigtheidsgolwe waargeneem.

Benewens was daar ook simulasies uitgevoer om die elektron diffraksiepatrone asook die strukturele data by kamer en lae temperature vas te pen. Die sagteware wat hiervoor gebruik word is genaamd Simulasie en Ontleding van Elektronendiffraksie (SAED) - Simulation and Analysis of Electron Diffraction (SAED).

Osituovidi

Imatiriya anahi turayi ileya ati cojenayidi mi mukoro inanin. Avuwere ka imatiriyononi obirenyi evini anayika anyéngwu tempirecho onuwa me kongwu de shebira osa suzu. Ebira owowa ono si zu ani ora me kahini ani sayénsi ényi akeyi ani hu nu irayi ébé va ani.

Aguvi ka itékiniki irenyi irenyi ara ero yi matairiyononi, inoyi nyakeyi ani, éyi va si tékiniki osa nyakeyi ani. Itékiniki ononi ahi ira anayi kaka omehura poro duwajeyi ovosiparahu. Isirononi ame ovi ka yehuó tura imatiriya ononi dóó shóó anka i foto avo. Hu ni foto ononi ya nyegwu nya keyi isa anana in ebirowowa oni ire. Di yere ebira owowa ononi ya bedo hunene pataki.

Isofiti wiye anahi simileshoni ati elekturoni yéré ro si nyakeyi imatiriya ononi. Ebira owowa enere ini ekisipériménti yéré re ini isofiti wiye ononi.

Ekura ononi vanayi inebira (This language is in Ebira).

Acknowledgements

All praise belongs to Allah who has made this a reality for me. My gratitude thus goes to my entire family in particular Medina Suleiman, Ochu Suleiman and Engnr. Yaqub I. Suleiman for their moral support. My sincere appreciation goes to my supervisor Prof. Heinrich Schwoerer for his well-thought suggestions and dedication, my research colleagues in person of Olufemi Olaoye, Bart Smit, Nicolas Erasmus and others I may not be able to mention. I do warmly extend my gratitudes to the staff of physics department workshop for their ever presence in time of need.

My sincere gratitude also goes to the following organisations for their funding of this research: The African Institute of Mathematical Sciences (AIMS), the Stellenbosch University (SU), the African Laser Centre (ALC) and the National Research Foundation (NRF).

I want to reiterate that this work has been presented twice at the annual conference of South African Institute of Physics (SAIP) in oral and poster presentations in the year 2013 and 2014 respectively. A poster presentation (in February 2014) was made at the Abdus Salam International Centre for Theoretical Physics (ICTP) during the Winter College on Optics: Fundamentals of Photonics - Theory, Devices and Applications which saw it winning a first prize with over 50 posters presented and over 100 participants from across the world including reputable professors from across the field of photonics. The work has also received a first prize for the best oral presentation at the 7^{th} African Laser Centre Annual Workshop and 3^{rd} Moroccan Days on Nanoscience and Nanotechnology held in Rabat with reputable professors in attendance.

Dedications

I dedicate this work to the peace of the world and hope that one day the world will recognise that an alternative to peace is destruction and therefore embraces peace as an inevitable option.

Contents

1. Introduction

In condensed matter physics, properties of solids such as electrical or thermal conductivity, magnetic susceptibility etc. could determine the nature of the solids as either insulators, conductors, semi-metal, semiconductor or superconductors and have been widely studied. Over the years however, interest has been shifted to rather what one may call "unorthodox" solids whose properties may undergo peculiar/or interesting phase transitions by changing parameters like temperature, pressure or photo-induced. Such solids often have strong electron-electron interaction or electron-phonon coupling. In other words they are regarded as strongly correlated materials and are usually quasi one dimensional or quasi two dimensional in nature.

One such type of strong electron-phonon coupling material that exhibits different phases based on the surrounding condition are trilayered inorganic compounds belonging to transition metal dichalcogenides. There exists different polytypes of these trilayered compounds that have generally been studied. One polytype that has received particular attention for about four decades is the 1T-$TiSe_2$ (one T-titanium diselenide) and it is the main focus of this thesis.

1T-$TiSe_2$ undergoes a second order phase transition due to a temperature change. This second order phase transition occurs in the crystal at around 200 K or below where a doubling of the lattice constant occurs along the a, b and c crystal axis resulting in a commensurate superlattice known as charge density waves (CDWs). Because the Fermi surface plays a major role in determining the properties of most solids, 1T-$TiSe_2$ is no exception. Therefore, the CDW formation is as a result of an opening of a band gap in the electronic structure at the Fermi surface resulting in a change of electrical conductivity. The occurrence nature of the CDWs however have remained a point of controversy as well as a point of interest as the physical mechanism driving the formation is yet undetermined.

Charge density waves are so called because they form standing waves in a crystal. These waves dictate what potential the ions residing in the crystal experience thereby leading to a change in equilibrium position of the ions and a periodic lattice distortion (PLD) is initiated. Because there are conduction electrons present in the crystal as one would expect, these conduction electrons would want to screen the new potential created and are themselves modulated. This modulated electron density is the CDW. In the 1T-$TiSe_2$, there are claims

that both PLD and CDWs are simultaneously occurring with the former driving the latter. However, these claims have met strong opposition from those claiming that the formation of the CDWs is purely of electronic origin with no periodic lattice distortion or that if any, could have been "accidental". In the mean time, as argument rages on about the driving force behind the charge density wave (CDW) formation the nature of the crystal itself was called into question as it is either a semi-metal [1] or semiconductor [2] at room temperature and semi-metal [3] or semiconducting upon transition temperature.

There are different models that can be used to describe CDW formation in materials characterised by electron-electron and electron-phonon interactions. These include Mott insulators, excitonic insulators and Peierls insulators [4]. The last two models have been used to describe the formation of the CDWs in the 1T-$TiSe_2$ and have actually led to the controversies explained above. These two models will be explained in Chapter 2.

Different experimental and theoretical tools have been used to study this crystal and they include steady-state measurement based on transmission electron microscopy by Woo *et al.*, x-ray scattering, Angle-resolved photo-emission spectroscopy etc. with majority of these focusing on the electronic structure of the crystal or band structure calculation. In all of these studies, there is a general agreement that commensurate superstructures or (CDWs) occur at around 200 K or below leading to the doubling of the three crystal axes but not so for the mechanism driving the formation of these superstructures as pointed out earlier.

My project therefore is to use a different experimental tool based on femtosecond time-resolved electron diffraction to study the crystal because we would like to have a much greater insight into its structural evolution on atomic scales. Such an insight could perhaps be critical to understanding the physical driving force behind the superstructure formation.

At this point, it is important to give a brief introduction into the working principle of the femtosecond electron diffraction technique. Since we want to study the structural dynamics of our crystal on an atomic scale, it requires that such structures be studied on a short timescale on the order of 10^{-13} s. A timescale equivalent to a lattice vibrational period hence the use of a femtosecond laser or in a lay man term a very short pulse of light. So we have a femtosecond laser source that is split by a beam splitter into two, namely: a pump and a probe laser. The pump laser excites the crystal in terms of energy deposition and the probe laser takes the snap shot of the structure initiated by the pump laser. Because we use electrons as a probe instead of laser, the probe laser is then frequency tripled into an ultra violet (UV) pulse that is used to generate electrons from a gold photo-cathode. The pulse duration of the electrons is the same as the incident UV laser. The crystal being photo-excited by the pump laser and the snap shot by the probe laser (in this case the electron pulse) is then obtained as an electron diffraction signal. A delay between the pump and the probe pulse gives the time aspect of this technique that makes it possible to observe in time the evolution of the structure. Hence time-resolved femtosecond electron diffraction. The diffraction signals carry information about the structure and can be retrieved by careful analysis of the signal.

We have successfully used this technique to generate the electron diffraction pattern of our crystal at room and low temperature and the signature of the CDWs observed at around 200 K or below. The structural dynamics of the crystal based on time-resolved femtosecond electron diffraction have been obtained for Bragg and CDW spots. Steady-state temperature characterisation of the Bragg and CDW intensities have been carried out. The results chapter gives the full insight and discussion of these results. It is important to emphasize that this is the first time that an initial experiment on this crystal has ever been performed based on this technique.

Another important tool that can be used to understand qualitatively the room temperature and low temperature phases of this crystal is a simulation tool. By using this tool, an electron diffraction pattern can be obtained. One such simulation tool that we have used is the Simulation and Analysis of Electron Diffraction (SAED) software [5]. Besides the crystal structure which has to be provided, experimental parameters such as electron acceleration voltage and the thickness of the sample can be specified with the exception of temperature. The incorporation of temperature parameter is now based on the structural information of the crystal that is available for room temperature as well as low temperature. The low temperature structural data available was at 77 K obtained from [1]. The atomic coordinates for the low temperature have been reconstructed from the room temperature atomic coordinates [6, 7] based on the atomic displacement given in [1]. When given all these parameters together with the space groups of the respective phases an electron diffraction pattern is generated. We have generated such an electron diffraction pattern for both the room and low temperature phases. The low temperature phase is the temperature for which the structural refinement of the crystal was performed and it was at 77 K [1]. All of these have been presented in detail again in the result chapter.

The chapters in this thesis have been organised as follows: Chapter 2 gives a great in-depth into the theoretical background. Chapter 3 discusses the experimental tools that have been used, Chapter 4 highlights the sample preparation procedures, Chapter 5 gives a general overview of measurement procedures for a successful experiment, the results and discussions for both simulation and experiment are presented in Chapter 6 and the summary in Chapter 7.

2. Background Theory of Charge Density Waves

In the world of solids, different models have been used in the past to describe their state. Such models are the Drude and the Sommerfeld models. Both models are based on the same idea - free electron. However, whilst the former considered metals to possess positive ions as cores in a lattice with the electrons freely moving between these cores thus neglecting any form of electron interaction with the lattice, the latter proposed that indeed the ion cores present in the lattice create some sort of potentials due to lattice periodicity created by electron interaction with the lattice leading to the creation of a band gap. Nonetheless, both models have been successful in explaining certain observed properties in metals. The Drude model for example has failed to explain the properties of solids such as the electronic heat capacity and thermal conductivity whilst the Sommerfeld model could explain the various states of some solids such as insulator, semi conductor, semi-metal or metal, a feature mainly due to an interaction between the free electrons and the lattice ion cores (i.e., its generated periodic potential is taken into consideration). Materials that exhibit new features different from the 'naturally' occurring features have been discovered in the past four decades including organic and inorganic materials. They exhibit exotic features known as charge density waves (CDWs). Such materials are classified as strongly correlated materials due to the strong interaction of their electrons with each other and/or lattice. In this kind of materials, the above mentioned models could not be used in the description of the observed phenomena hence models such as the Mott instability, excitonic instability as well as the the Peierls instability are used. See Section 2.2.1 and 2.2.2 for the explanation of the last two models.

In our ultrafast electron diffraction group, some of these correlated materials have been investigated. They are the highly studied set of inorganic layered compounds of different polytypes known as the transition metal dichalcogenides (TMDCs). Those studied in our group include the $4H_b$-$TaSe_2$ and $1T$-TaS_2 [8–10]. My thesis therefore focuses on a different member known as $1T$-$TiSe_2$ as introduced earlier in Chapter 1. The $1T$-$TiSe_2$ has been the highly studied polytype amongst the sets of the TMDCs mainly due to the difficulty in establishing the driving mechanism behind its charge density wave formation and more recently the pressure-induced superconductivity observed in the crystal [11] and its copper-

intercalated upon cooling [12] has steered further interest.

2.1 Charge Density Waves Formation

If we recall the Sommerfeld model explained earlier where due to the electron-lattice interaction there is the formation of a band gap, in a similar manner does the formation of charge density waves lead to a band gap formation at the Fermi surface but only when certain conditions are met - the process has to be energetically favourable under such conditions since the band gap formation does not occur 'naturally' in these correlated materials. CDWs formation usually occur due to the modulation of the electron density by the ionic periodic potential. The ions in the crystal thus see different potentials causing a distortion in the lattice periodicity. This simultaneous occurrence of two processes is called the charge density waves with periodic lattice distortion (PLD). This new periodicity (CDW) thus opens up a band gap (energy gap) at the Fermi level.

We mentioned earlier that this process does not come by easily in these types of materials. Let us then look at what the system must satisfy in order to exhibit these phenomena. The Fermi surface as we all know play a crucial role in the understanding of the band structure of solids. This is because the formation of a band gap occurs around the Fermi surface - evident in the Sommerfeld model. It would not however be surprising if we then point to the Fermi surface in the quest to explain the formation of a CDW gap.

Let us consider a one dimensional metal which has a uniform electron density distribution in its metallic state as depicted in Figure 2.1. For a CDW gap to form, there has to be an energy cost - a reduction in the total electronic energy. Since the band gap opens at the Fermi surface, it implies that the states residing below the Fermi level will have their energy lowered while raising the energy of the states residing above the Fermi level. In this manner, there is a gain in energy which then surpasses the energy utilised for a change in state (i.e., for a CDW state and gap formation). This is the Peierls instability which will be explained briefly again in section 2.2 and Figure 2.1 illustrates the Peierls instability/or CDW formation.

As indicated in the introduction to this chapter, my focus is on a strongly correlated material of a layered crystal known as 1T-$TiSe_2$. There is a hierarchy of three models of insulators that are generally used in describing gap formation in these kinds of materials. They include the Mott insulator, excitonic insulator and the Peierls insulator [4]. The CDW formation in 1T-$TiSe_2$ has been tied to two of these models: the excitonic instability or insulator and the Peierls instability or insulator. We shall therefore in the following section attempt to explain the CDW formation in the context of both of these mechanisms.

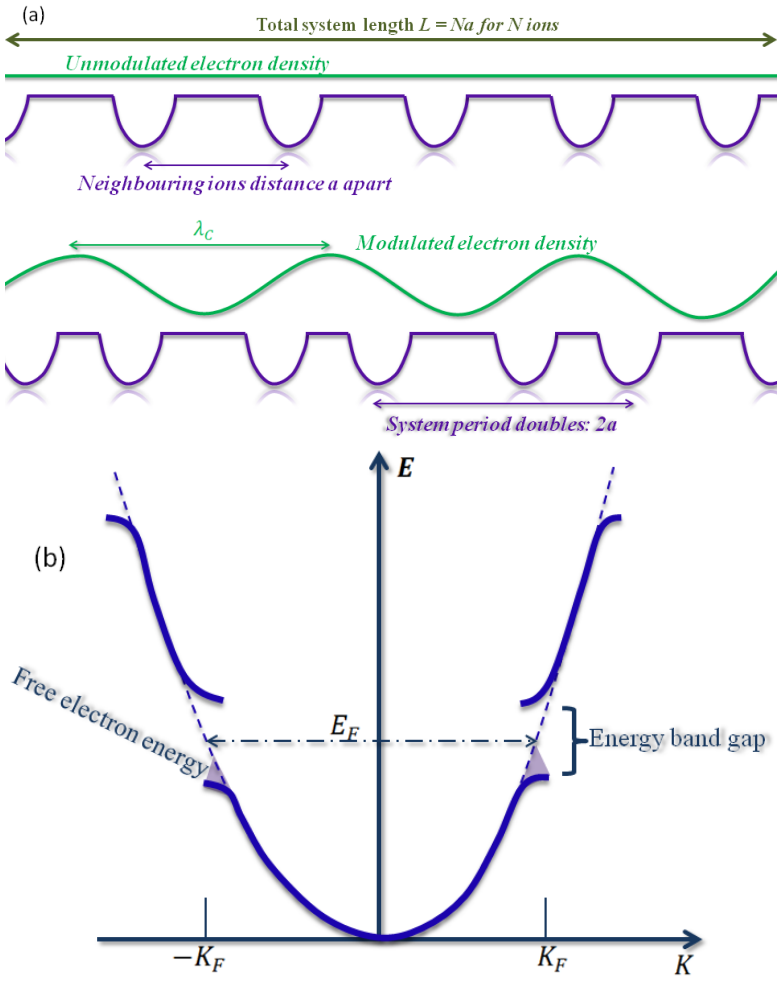

Figure 2.1: (a) Upper: Ionic potential seen by electrons in a system whose positions of atoms are unperturbed. This lattice potential partially reflects the electron waves at different wavelengths without any pronounced effect. Lower: Ionic potential seen by electrons where in this case the effect of the lattice potential modulates the electron density with its wavelength becoming twice the ion spacing. Such modulation of electron density causes what is referred to as charge density waves (CDWs). A periodic lattice distortion is thus initiated due to the effect of the modulation on the position of the atoms in the crystal. (b) The formation of the CDWs introduces a gap at the Fermi surface ($k = \pm k_F$) where the CDW wavevector, $q_{CDW} = 2k_F$. There is a total energy cost for a favourable and stable formation of the CDW gap. The whole of these processes can also be referred to as Peierls transition.

2.2 Proposed Models

Whilst the Drude or Sommerfeld models could explain certain states in some solids such as thermal or electrical conductivity, electronic heat capacity, electronic density of states etc. however these models could not explain the complexity (complexity such as the interaction between the electrons and/or the lattice) of the ground-state signatures observed in these kind of materials. Hence the need for models capable of describing the observed phenomena. The proposed models for 1T-$TiSe_2$ include the excitonic instability and the Peierls instability.

2.2.1 Excitonic Instability

Under certain circumstances for example at sufficiently low temperature, semiconductors with very small band gaps or semi-metals with a very small band overlap are prone to ex-

hibit this phase. Therefore, it is not surprising to see that its state is controversially classified as either a semiconductor [2] or a semi-metal [1]. The occurrence of excitonic insulator is primarily due to low carrier density so that interactions between the holes and the electrons are weakly screened leading to bound states of holes and electrons known as excitons. If the binding energy of such a bound state is larger than the energy gap, a negative energy is then required to create an exciton and this will lead to the instability of the ground-state of the system thereby leading to condensation of the exciton at a low temperature. The condensation thus forms the CDW and the resulting energy gap. This kind of CDW formation is said to be electronically driven. Hence such instability is usually described as electron-hole (or electron-electron) interaction or coupling with little or no periodic lattice distortion [4, 13].

2.2.2 Peierls Instability

A good illustrative example for Peierls instability is a one dimensional metal as indeed suggested by Peierls himself [14]. In such materials (this description of Peierls is also the same for the 1T-$TiSe_2$), we have the conduction electrons in states below the Fermi surface. Consequent upon cooling, a periodic lattice perturbation will force an opening of an energy gap at the Fermi surface thereby leading to a lower energy of the states as previously explained in section 2.1. As predicted by Peierls, such an energy gap would open when the wavevector accompanying the lattice deformation has its value equal $2\,k_F$ resulting in a CDW formation. This kind of instability is a consequence of strong electron-phonon (or electron-lattice) coupling. See refs. [15] for further in-depth explanation on both models.

2.3 1T-$TiSe_2$ as a Transition Metal Dichalcogenide (TMDC)

Structural Overview

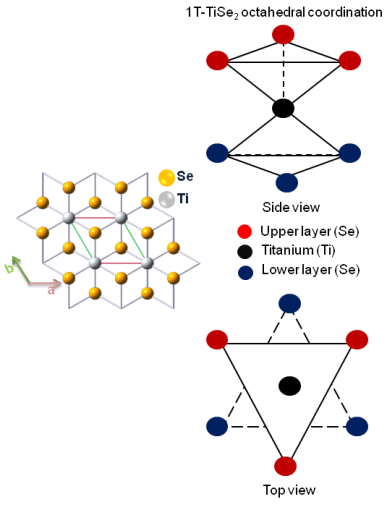

Figure 2.2: Left: A unit cell of 1T-$TiSe_2$ Right: Display of top and side views of the octahedral coordination in the unit cell.

The TMDCs are generally denoted as MX_2 where M represents a transition metal and X represents a chalcogen atom. For the crystal, M is the titanium atom, X is the selenium atom. The letter "T" denotes the polytype and it means it is trigonal and the number "1" represents how many sandwiches make up a unit cell [16]. One sandwich implies that there is a titanium atom layer sandwiched in between selenium atom layers classified as either lower selenium atom layer or upper selenium atom layer. 1T-$TiSe_2$ is generally agreed upon to undergo

a second order phase transition at ∼200 K [1, 17] or below 200 K [18] forming a commensurate $2\,a_\circ \times 2\,b_\circ \times 2\,c_\circ$ superstructure known as charge density waves. In this state, its space group is known to be $D^4_{3d}(p\bar{3}c1)$ and contains 24 atoms per unit cell [16, 19]. At room temperature, its lattice constants are given by a = b = 3.537 Å and c = 6.005 Å based on x-ray measurement [7] and a = b = 3.54 Å and c = 6.008 Å based on neutron diffraction [6]. It belongs to a space group $D^3_{3d}(p\bar{3}m1)$ at room temperature containing only three atoms per unit cell [16, 19].

Let us at this point depict the real-space unit cells at room temperature (normal phase) and low temperature (distorted phase) with their corresponding reciprocal phases to have a better visualisation of what charge density waves or superstructures are. Figure 2.3 and 2.4 depict the real-space unit cells of the crystal, the electron diffraction pattern from simulation and the electron diffraction pattern from experiment respectively for room and low temperature. The charge density wave spots can be clearly seen for the low temperature in Figure 2.4 (b) and (c) with the spots depicted in blue and grey as in (b).

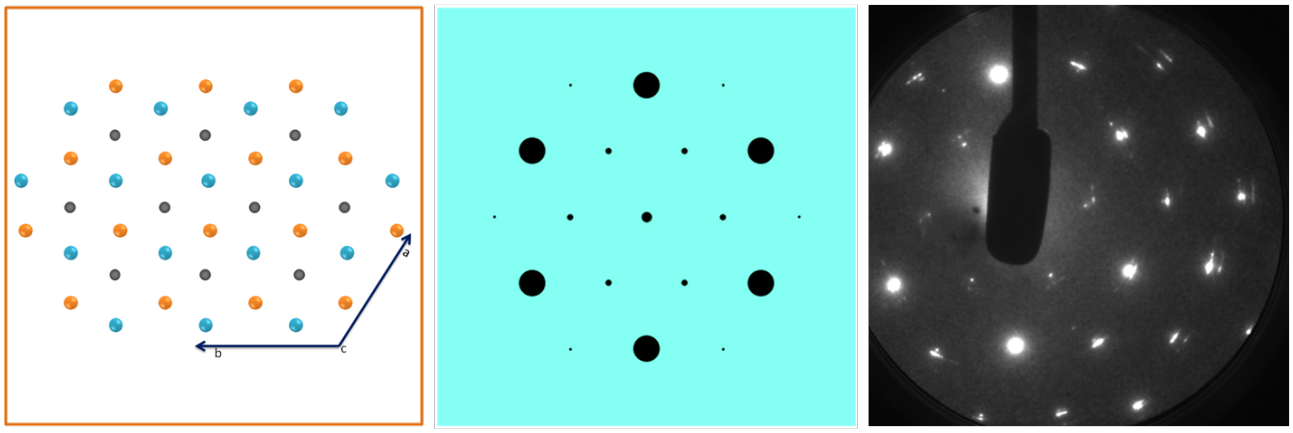

Figure 2.3: (a) A schematic representation of the real-space unit cells of the undistorted phase with the blue, orange and grey colours denoting the selenium upper layer, selenium lower layer and the titanium layer respectively. (b) Simulation showing the electron diffraction pattern at room temperature. The room temperature parameters are fed into the software and sample thickness of 30 nm and a high voltage of 30 kV are specified. The hexagonal structure of the crystal shows a strong signature in the generated pattern. The black spots are the Bragg spots with the bigger spots indicating a constructive interference resulting from where the electron density distribution is highest in the crystal. (c) Electron diffraction pattern of 1*T*-$TiSe_2$ obtained from measurement at room temperature and at 30 kV for a 30 nm thick sample. The white spots are the equivalence of the black spots in (b) which are also the Bragg spots. More higher orders are however revealed compared to that obtained from the simulated pattern.

This particular inorganic layered crystal under investigation in this thesis has been widely studied by several groups for about four decades who have used different theoretical and experimental tools. Despite the in-depth study on this layered material, the mechanism driving its CDW formation is still a controversy. Among these experimental tools include x-ray studies [7, 20–22], neutron diffraction [1, 6], electron diffraction [18] etc. which have focused mainly on the structural changes. Angle-resolved photo-emission spectroscopy (ARPES) [23–25], optical spectroscopy [18, 26], specific heat [27, 28], and transport measurement [29] etc. have focused also on the electronic properties and changes in the electronic spectrum of the crystal. Theoretical techniques on the other hand have utilised the tight binding model

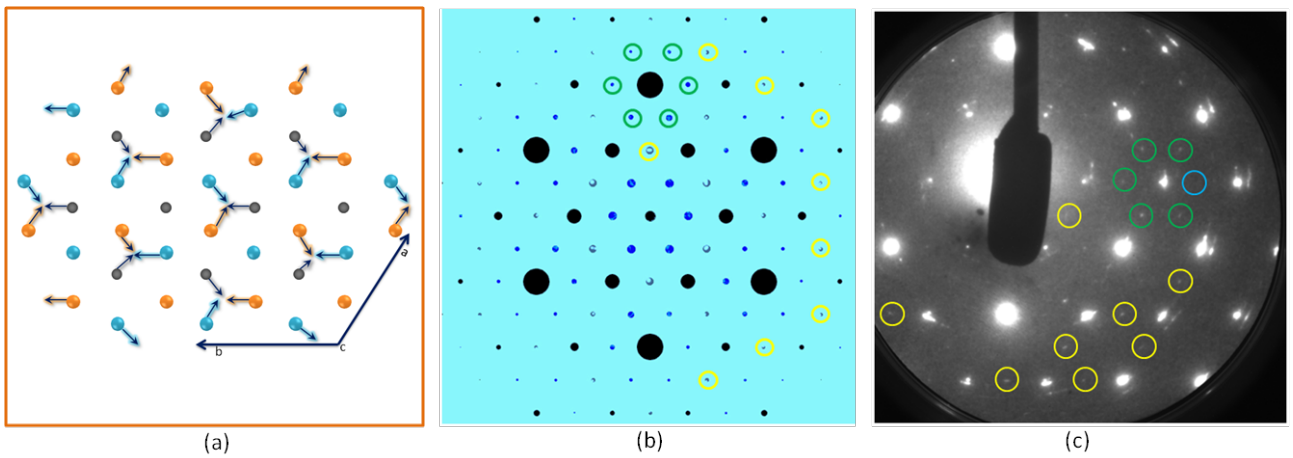

Figure 2.4: (a) A schematic representation of the real-space unit cells of the distorted phase with the blue, orange and grey colours denoting the selenium upper layer, selenium lower layer and the titanium layer respectively. Arrows indicating the displacements of atoms are not to scale. (b) Simulation showing the electron diffraction pattern at low temperature. The low temperature parameters are fed into the software and sample thickness of 30 nm and a high voltage of 30 kV are specified. The hexagonal structure of the crystal shows a strong signature in the generated pattern revealing the commensurate superstructure or CDW spots which are depicted as grey and blue spots which are mere colour notations of the peaks. The black spots are the Bragg spots with the bigger spots indicating a constructive interference resulting from where the electron density distribution is highest in the crystal. The green and yellow circles are used to indicate CDW peaks that have been observed in the experimental pattern. (c) Electron diffraction pattern of 1*T*-$TiSe_2$ obtained from measurements at low temperature and at 30 kV for a 30 nm thick sample. The pattern also bears the signature of the hexagonal structure of the crystal. The white spots are the equivalence of the black spots in (b) which are also the Bragg spots. The green and yellow circles are used to indicate CDW peaks that have been seen in the experiment as well as in the simulation with the blue circle indicating an absence of a CDW peak. The absence could be due to weaker amplitude of the peak or sample quality. The same higher orders are revealed in both simulation and experiment contrary to Figure 2.3 (b).

mainly to look at the electronic structure near the Fermi level [15]. A few time-resolved measurements have also been done and they include time-resolved optical reflectivity, time-resolved x-ray diffraction [22] and time-resolved ARPES [4].

It will however be interesting to briefly highlight the findings involving some of these techniques. We stated earlier that the main controversy about this specific sample is the mechanism driving its CDW formation and that two models have thus been proposed to explain this phenomenon. Some of these findings however have either supported the excitonic or Peierls model. For example, detailed study on the energy band structure by [30] has revealed that 1*T*-$TiSe_2$ is a semi-metal and a band gap of $\sim 0.2 \pm 0.1$ eV by Chen *et al.* has been obtained [31]. This is in contrary to Rasch *et al.* who argued for a semiconductor with a small indirect band gap [2]. In a separate work [1], Di Salvo *et al.* considered the 1*T*-$TiSe_2$ as a semi-metal - a view supporting an electron-hole (electron-electron) e^-–h^+(e^-–e^-) driven transition. The observed transverse atomic displacement at the transition temperature together with a reduction in hole concentration upon deviation from stoichiometry strongly support their claim. A new high resolution ARPES study by Cercellier *et al.* [23] also favours the excitonic model arguing that the $2\,a_\circ \times 2\,b_\circ \times 2\,c_\circ$ superlattice formation along with the partial opening of a gap are driven purely electronically. Not only that, the high resolution ARPES study, which according to Cercellier *et al.* agrees quite well with theoretical calculations, has shown a back-folded band with large spectral in the CDW phase. This observation cannot be attributed to an atomic displacement associated with Jahn-Teller effect [32] but with a system whose CDW formation is electronically driven.

Time-resolved optical reflectivity by Vorobeva *et al.* [22] reveals a frequency rise of 3.4 THz at low temperatures and this is attributed to one of the amplitude modes of the superstructure. The associated oscillations are highly dependent on the fluence used with a complete disappearance of the superstructure at a fluence of 0.21 mJ/cm^2 for a sample at 80 K. This observation has been attributed to laser induced melting of the CDW superstructure. This is in agreement with a result from a trARPES measurement by Hellmann *et al.* [4] where the coherent amplitude oscillations in the spectral response are completely suppressed at higher excitation densities. This observation by Hellmann *et al.* is also consistent with the study by Rohwer *et al.* where there is a dependence of the melting time of a superstructure peak based on the excitation density used - a unique attribute of electronic structure dynamics of 1T-$TiSe_2$ [4]. Both results have pointed to excitonic instability with a caution however from the Hellmann group that only dominant characteristics due to melting of the phase and not the driving mechanism has been studied.

Vorobeva *et al.* [22] has performed a transient measurement based on x-ray diffraction to further ascertain their claim of a non-thermal disappearance of the superstructures. According to the group, a successful photo-excitation with a range of specific pump fluences shows a decrease in the CDW signal generally due to atomic rearrangement resulting from a laser-perturbed electronic order of the system. A range of pump fluences from 0.15-0.24 mJ/cm^2, depending on the temperature of the sample, sees a rapid drop in the CDW signal with a ps recovery time whilst a pump fluence of around 1.2 mJ/cm^2 sees a complete suppression of the superstructure with a longer recovery time attributed to a transition to the normal (room temperature) phase of the sample. What is quite interesting about this study is that detailed quantitative determination also points to a melting of the CDW structure induced by laser irradiation - a signature of electronic processes driving the CDW in 1T-$TiSe_2$. This claim is made in relation to the quantitative similarity observed between the condensation energy of the CDW state and the threshold energy necessary for the collapse of the CDW structure. A possible thermal origin from laser induced heating resulting in the collapse of the CDW structure has been ruled out by the group as the threshold energy for thermal melting was too high. This study yet again supports the excitonic insulator model. This observation of a threshold energy resulting from the threshold fluence required to melt the CDW superstructure non-thermally is contrary to the excitation density required in the trARPES [4] for non-thermal melting. Despite this difference, both studies point to the excitonic instability as the dominant character. For more on those supporting this model please refer to [13, 33–35]

Others have attributed the driving mechanism to the Peierls transition mainly due to the observed lattice distortion [36, 37]. A more cautious approach is taken by van Wezel *et al.* [38] who have proposed that both models could be a combined driving mechanism i.e., exciton-phonon (exciton-Jahn-Teller). A claim he based on a tight binding model which explicitly explains that a weakly connected quasi one dimensional chain of the 3d orbitals in 1T-$TiSe_2$ and its surrounding Se 4p play a major role in the observed phenomena. For a complete review on the state of this layered crystal see ref. [15].

Our interest is thus to investigate this sample using a tool that can track the structural evolution in time. In other words, we want to study the structural dynamics of the crystal as it evolves on atomic scales. To study such dynamics on atomic scales, we use a technique known as pump-probe based on femtosecond electron diffraction. The interesting parameters about this technique are its temporal and spatial resolutions which are on the order of 500 fs and 10 nm respectively. We have a pump laser which initiates the structural dynamical processes and a probe electron pulse takes the snap short of these processes. With this technique, an electron diffraction pattern associated with a specific crystal can be generated. Information about the crystal can thus be retrieved from diffraction spots of the sample. Whilst we are not the first to use time-resolved tools, however, to the best of our knowledge we might be the first to carry out a time-resolved electron diffraction measurement on this particular layered compound based on a pump-probe technique. It is important to note that our goal is to contribute our quota to the pool of scientific knowledge already available on this crystal and not to categorically state which model could best describe the observed physical processes driving its CDWs. In the next chapter, the experimental tools used to investigate this crystal shall be discussed briefly.

3. Experimental Setup

The major experimental components necessary to set up an ultrafast electron diffraction (UED) are 1) a femtosecond laser system, 2) an optical beam splitter, 3) an ultrafast electron gun, 4) an electron optic such as a magnetic solenoid lens, 5) a vacuum chamber, and 6) a detector. The schematic of the various components of a typical UED setup is shown in Figure 3.1. Though, a thorough and detailed explanation of all the components listed here has been given in [9, 10]. We shall therefore attempt to give a brief insight into the working principle of the listed components by starting sequentially.

3.1 UED Components

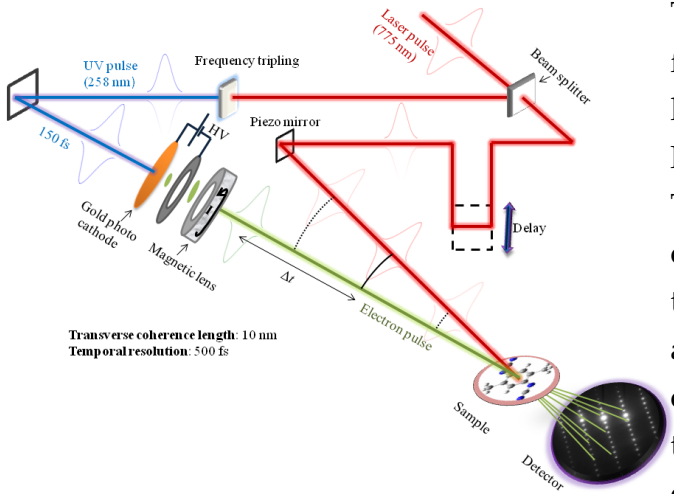

Figure 3.1: Schematic representation of an ultrafast electron diffraction setup for a pump-probe technique.

Femtosecond Laser System

The femtosecond laser laboratory for ultrafast electron diffraction is equipped with a laser system of model CPA2101 by Clark MXR. The CPA2101 laser system is a Ti:Sapphire laser that produces short pulses of laser in the femtosecond regime. Parameters worth mentioning of the CPA2101 laser are its pulse energy which is on the order of 800 µJ, pulse duration of 150 fs, repetition rate of 1 kHz and central wavelength of 775 nm. Since the laser system is shared with other groups, we only take around 200 µJ of the pulse energy.

Optical Beam Splitter

Because the experimental concept is based on a pump-probe technique, an optical tool is thus required to achieve this. This is where the optical beam splitter comes in to play. The optical beam splitter is a very crucial optical device in pump-probe spectroscopy. It is a semitransparent device that splits a beam of light into two parts. Our 775 nm laser pulse

in this case is split into 50:50 pulses: a pump and a probe laser pulse as in Figure 3.1. The probe (UV) pulse intensity can then be controlled using a variable filter which is usually set to transmit 9 % or 17 % of the incident UV pulse as the case may be. This is to ensure that the photo-cathode is not damaged due to high UV pulse intensity.

The Ultrafast Electron Gun

In order to fully achieve the pump-probe setup for an ultrafast time-resolved electron diffraction experiment, a device is required to generate an ultrashort pulse of electrons. Such a device is the electron gun. This is so-called because its geometry is comparable to that of a gun. The probe pulse is aligned to two beta barium borate crystals (BBO) containing a half-wave plate sandwiched in between. The first BBO crystal frequency doubles the probe pulse (the probe pulse in this case is the laser pulse before conversion to UV) creation. The half-wave plate orients the polarisation of the beam before it passes through the second BBO crystal hence we have a sum frequency of the fundamental and two photons. One of the photons is the third harmonic which we are interested in. Note that all of these processes have been depicted by the label "frequency tripling" in Figure 3.1. The mechanism leading up to the tripled frequency is simple. Since BBO is a non-linear crystal it means that as the probe pulse is aligned to the first BBO, the wave of the fundamental creates a non-linear polarization wave due to the non-linearity of the crystal. The non-linear polarization then oscillates at twice the frequency of the fundamental so that with good phase matching the field created by the non-linear polarization wave propagates with dominance in the same direction as the wave. The fundamental wave is thus attenuated due to interaction with the non-linear polarization wave. The second harmonic passes through a half-wave plate positioned perpendicularly to the input beam. The half-wave plate ensures that the linearly polarized beam stays linear if the polarisation direction is along one of the axes of the half-wave plate before it passes again through the second BBO crystal (sum frequency) i.e., two photons (the fundamental and the second harmonic) are destroyed to create a single photon having a frequency three times that of the input beam. Since both the fundamental, the second and the third harmonics travel through the BBO, a prism is then used to separate the three wavelengths from which only the third harmonic is selected and the rest (fundamental and second harmonic) blocked.

The third harmonic (UV) pulse is directed to a lens of focal length 30 cm situated just before the gun's beam entrance window. The electron gun houses the cathode and the anode and only connects to the main chamber through the anode hole. The reason for frequency doubling or tripling is because of the type of metal which the cathode's surface may be coated with as the energy of the photon has to be sufficient to generate electrons from the cathode's surface. In our laboratory, the cathode is coated with a thin gold layer on the order of 10 nm thick. Hence, the frequency tripled laser pulse with a wavelength of $\sim$258 nm corresponding to an energy of $\sim$4.8 eV is just sufficient to overcome the work function of the gold layer so that the generation of electron pulses is possible. This process is simply the photoelectric

effect. The advantage associated with using a gold layer is the facilitation of easy transfer of electrons to the surface of the cathode already charged to a potential of -30 kV. The electrons are then accelerated by a high electric field established between the cathode and the grounded anode through an anode hole of about 2 mm. The accelerating distance (cathode-anode gap) is just about 4 mm, which implies that the electrons are accelerated by a field of 7.5 kV/mm.

Such a high voltage is suitable for our particular diffraction geometry. For instance, to limit the energy spread of our electron pulse an acceleration field strength of around 7.5 kV/mm or 10 kV/mm is necessary. This means that a short acceleration distance is also required as a longer distance leads to a decrease in the strength of the acceleration field. Because electron diffraction makes use of the wave nature of electrons which technically occurs as a result of electron interaction with a matter thereby forming an interference pattern, it therefore means that the de Broglie wavelength should not be larger than the inter-atomic spacing of matter if a diffraction pattern needs be observed. Typically, the inter-atomic spacing of solids is a few Angstroms. Hence, a wavelength of 0.07 Å which corresponds to a kinetic energy of non-relativistic electrons is satisfactory for electron diffraction. All of these parameters are interwoven and have been carefully chosen to suit our diffraction setup.

Electron Optics (Magnetic Lens)

Once the electron pulses are accelerated through the anode hole, the next step is to focus these fast travelling electron pulses onto the target sample and/or the detector. This is because there is a space charge broadening (electron spread-out in space) due to field distributions between the electrons as they propagate through space (see Section 3.2 for space charge effect). Hence the use of magnetic lens for focusing the electron beam to the target sample. The role however, should not be mistaken for the prevention of energy spread and space charge broadening of the electron bunches. Two types of electron optics can be used to achieve this purpose: electrostatic lens and magnetic lens. Whilst we use the latter in our setup, we do not use the former due to high electrode potential required [39]. The magnetic lens consists of a circular coil wound around a casing with a circular opening of 6 mm in diameter and 18 mm in thickness. The circular coil generates the magnetic field when current runs through it. As the electrons pass through the field, they experience a Lorentz force directed towards the axis. This so happens because of the interaction of the azimuthal velocity of the electrons with the axial magnetic field. As the electrons exit the solenoid field, the azimuthal velocity of the electrons fade off resulting in a focused electron beam. The heat generated by the lens is dissipated via an aluminium mount which is thermally coupled to the chamber base plate serving as a heat sink. See Appendix A.5 Figure A.3 for the magnetic lens.

Vacuum Chamber

The vacuum chamber has a hexagonal stainless steel frame with six side plates made of aluminium that host the windows, feedthroughs and detector flanges. Inside the chamber, the gaseous pressure is about 10^{-6} mbar. The chamber is connected to a turbo pump and a rough pump. The rough pump achieves a pressure of about 10^{-2} mbar which removes some of the atmospheric gas. However, this pressure is too high and as such, it is in turn connected to a turbo pump so that the vacuum chamber provides an over all pressure of about 10^{-6} mbar. The turbo pump (Oerlikon Turbovac SL700) has a pumping capacity of $700\,\mathrm{l/s^{-1}}$. The vacuum chamber is designed to be as flexible as possible. Necessary protocols are taken to ensure that all components used in the chamber are properly cleaned ultrasonically with the appropriate solvent and are vacuum compatible. Recently, a vacuum pump was attached to the electron gun to further enhance the vacuum in the gun.

The vacuum system is necessary because it houses such components as the microchannel plate (MCP), the phosphor screen detector, the magnetic solenoid lens, and the electron gun where no arcing should take place. Especially the MCP needs a low pressure, on the order of 10^{-5} mbar, because the MCP is highly hygroscopic meaning that water vapour is easily absorbed by the MCP. Once that happens it decreases the performance of the detector. Another necessity of the vacuum is that electrons are easily propagated in free space (vacuum). The electrons are generated in the electron gun and are accelerated with a high voltage. See Appendix A.5 Figure A.2 for the full view of the chamber.

Detector

The basic components that make up the electron detection system are a phosphor screen, a charge coupled device (CCD), and a microchannel plate (MCP). With the integration of these systems, a diffraction signal from a given sample is obtained. The MCP functions as an electron multiplier. The electrons scattered off the sample are collected by the MCP which amplifies the signal before being directed onto the phosphor screen. The phosphor atoms get excited and then emit some photons. These photons are then imaged by the lens employed in our laboratory (Nikon AF-SMicro60mmf/2.8) onto a 16 bit CCD camera. The typical operating voltage of the MCP together with the fluorescence stage is in the range of 4300 V-4500 V. The spatial resolution of the MCP is also an important aspect and its channel diameter and centre-to-centre (c-c) spacing which in our case is 12 µm (15 µm c-c) determine our MCP resolution. Because the output of our MCP is observed with a phosphor screen, it means that the electrode depth penetration, the space between the MCP and the phosphor screen as well as the accelerating voltage determine the spatial resolution. Spatial resolution is also known to be less in a stacked MCP, two matched MCPs in V-stack known as Chevron assembly, as is our case. Thus, with an active diameter of 40 mm and the distance between the sample to the detector (MCP) being 340 mm we are limited to detection angles in the range $0.699^\circ \leq \theta \leq 1.668^\circ$ corresponding to k-vectors in the range $0.35\,\text{Å}^{-1} \leq k \leq 0.83\,\text{Å}^{-1}$ respectively for the first order peaks and for an accelerating voltage of 30 kV.

See [9, 10] for more detailed explanation on these systems as well as how the pump and probe beam can be corrected for during an experiment and how the pump and probe beam profile can be measured.

3.2 Space Charge Broadening

Coulomb repulsion is one of the problems associated with putting many electrons together. In our group, understanding the behaviour of these electrons as they propagate through space was championed by Kassier in his PhD thesis [39], a study that led to the design of our electron gun and vacuum chamber with which all the experiments in our group are being performed. Using ASTRA code together with the required parameters, he demonstrated the broadening of an electron pulse due to Coulomb repulsion. Table 3.1 shows some of the parameters incorporated in the code and Figure 3.2 shows the simulation result as obtained by Kassier.

	Design choices
Acceleration energy	30 keV
Acceleration distance	4 mm
Initial pulse duration	150 fs FWHM
Initial spot size	35 μm FWHM
Cathode-sample distance	30 mm
Extraction opening	2 mm
Magnetic lens	hole diameter: 6 mm, thickness: 18 mm

Table 3.1: Design choices on which the electron gun was built [39].

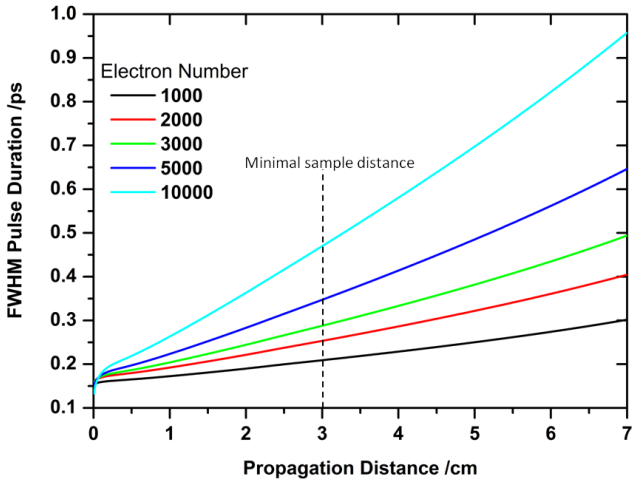

Figure 3.2: Simulated FWHM pulse duration versus propagation distance for various bunch charges. Rapid temporal broadening of the pulses is evident as the electron number per pulse is increased from 10^3 to 10^4. This has been re-simulated using some of the parameters specified in [39] or in Table 3.1. Note that an initial spot size of 25 μm and electron energy of 35 keV were used contrary to the ones used in the table.

The initial pulse duration used in the simulation is 150 fs which is reasonable since our pulse duration is in that range. It is obvious from Figure 3.2 that as the electron number increases the Coulomb repulsion also increases leading to the broadening of the pulse length. The broadening of the pulse length is seen to slowly set in as the electron propagates through space. The broadening of the pulse becomes more pronounced beyond a propagation distance of 30 mm as the electron number increases. This means that if one wants to achieve a high temporal resolution, the distance of the sample from the electron source has to be kept to a distance at which a good pulse length is obtainable. For example, 450 fs pulse duration is obtainable for as many electrons as 10000 electrons per pulse if the sample is kept to a distance of 30 mm. Since both electron numbers and propagation distance play a significant role in the temporal broadening of the electron pulse, it was taken into consideration in the whole design. The distance between the cathode and the sample was kept as short as 30 mm and the electron number kept low. Pulse duration of 180 fs for $1000e^-$ and 350 fs for $5000e^-$ can be obtained at this sample distance.

With the conception of a new ultra-high vacuum design reaching at least 10^{-9} mbar, it was necessary that the electron gun be optimised from the previous design. Also, achieving a very high temporal resolution is still a major challenge in the ultrafast electron diffraction field. Therefore to better understand the behaviour of electron pulses when they propagate it was necessary to further investigate the previous parameters used. This project is currently championed by a Masters' student in our research group. Figure 3.3 highlights one of the parameters investigated - the UV pulse spot size on the photo-cathode.

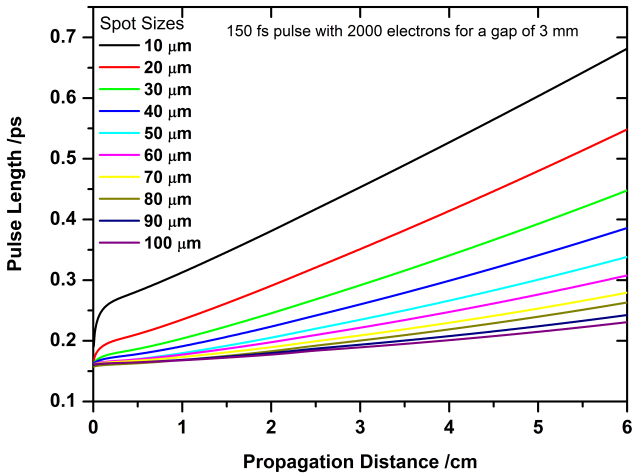

Figure 3.3: Simulated FWHM temporal duration versus propagation distance for various spot sizes. Rapid temporal broadening of the pulses is evident as the spot size is increased from 10 μm to 100 μm.

Electron number per pulse was limited to 2000 with a slight change in the acceleration distance to 3 mm for different spot sizes keeping all other parameters in Table 3.1 the same. Clearly, apart from electron number per pulse the initial spot sizes of the pulse on a photocathode also plays a vital role. A large temporal broadening is observed for a spot size of 10 μm. The idea is the same. The more electrons are confined to a very small volume, the

more they repel one another leading to temporal spreading. A pulse length of up to 200 fs or less for a propagation distance of 30 mm can be achieved from spot sizes of 70 μm to 100 μm respectively. However, there is a limit to which the spot sizes can be increased even though it leads to shorter pulse duration. Large spot sizes lead to loss in transverse coherence resulting in poor spatial resolution. See refs. [9, 10, 39] for more on transverse coherence. Therefore, a spot size of 30 μ could yield a pulse duration of around 300 fs or less for the number of electrons treated in this simulation and will be implemented in the new design.

3.3 Fundamentals of Diffraction

According to [40], "diffraction is a phenomenon that is caused by medium features that are small compared to the wavelength of the wave". Diffraction has been studied well using a light source. Such notable contributions to the development of diffraction theory came from the work of Francisco Maria Grimaldi who in the 1600s performed two sets of experiments where the result of the experiments was contradictory to geometrical optics. He coined the word "diffraction". Christiaan Huygen was rather obsessed with the wave theory of light based on diffraction. Another notable contributions made to the diffraction theory was the Young's experiment from Thomas Young where he gave "a proof of the general law of the interference of two portions of light" (recall the famous Young's single or double slit experiment). Augustin Jean Fresnel used the basis of Huygen's work to synthesise wave theory of light and interference having claimed no prior knowledge to Young's work. This work by Fresnel earned him the Grand Prix in 1819 from the French Academy of Sciences. Following Fresnel's success, Helmholtz, Kirchhoff, Rayleigh and Sommerfeld formed the mathematical explanation to these findings as a contribution to the continued development of the diffraction theory [40]. The wave and particle nature of light was also heavily contended. Diffraction of electron beams from a nickel crystal in 1927 by Clinton Davisson and Lester Germer demonstrated the wave nature of particles for the first time together with that of George Thompson with his thin films of celluloid [41].

Meanwhile, before Davisson's and Thompson's diffraction, W. H. and W. L. Bragg in 1913 observed a rather strange phenomenon of some substances when impinged with by x-rays. These substances which gave characteristic patterns of reflected x-ray radiation were classified to be crystalline. Hence the idea of diffraction as a tool to explore the underlying properties of some materials which are particularly crystalline in nature hit the mark. However, as great as these scientific milestones were, they do not provide information about the dynamical processes of the structure. In addition, sample structural damage has always been an issue. This is due to a demand in higher resolution which results in high energy deposition on the sample surface. The same problem is associated with electron microscopy. With the advent of the laser, this problem could be managed due to a high temporal resolution. A short laser pulse is employed as a source for x-ray generation which sends short packets of

x-rays. The same applies to electron pulse generation which also uses short laser pulses as a source. Hence, electrons generated in this manner are called ultrafast x-ray pulses and ultrafast electron pulses both used as probes respectively [42] and together have played a major role in diffraction. With these two techniques, high energy deposition was solved. It does not however solve the lingering questions about the observation of dynamical structural changes that take place on an atomic scale. So what then should be considered to achieve this? The answer to this question is discussed in section 3.4.

3.4 Diffraction as Time-Resolved

Structural dynamics of materials on atomic scales have become a leading frontier in the field of spectroscopy since femtosecond (fs) lasers were invented. Coherent structural changes of materials occur on a very short timescale equivalent to atomic vibrational periods which is on the order of 10^{-13} s or 100 fs, and this accounts for phase transitions in solids and perhaps other processes. Hence the use of ultrafast spectroscopy to study ultrafast structural dynamics for better insight into the material structures at this timescale. The study of such dynamical structural changes has employed the use of femtosecond (fs) pump and probe techniques. With these techniques, evolution of material structures can then be tracked in time at atomic scales. Indeed, this was considered as a major breakthrough in the field of spectroscopy.

The time-resolved diffraction experiments that have attracted most attention are the x-ray time-resolved and electron time-resolved diffraction experiments. Since the time x-rays were first used to perform diffraction experiments in the early 1900, attempts have been made to produce a femtosecond x-ray pulse using for example, laser-driven x-ray diodes. Just like the conventional way of producing x-rays in which a high potential electrode is connected to a metal target situated in a vacuum, the same principle applies but in this case it is achieved via an ultrashort electron pulse produced by the photoelectric effect which is then accelerated towards a metal target generating pulses of x-rays. The x-rays produced has the same temporal resolution as its source generator (i.e., the electron pulse). Similar attempts have been made towards generating a femtosecond laser based ultrashort electron pulse. The femtosecond laser pulse which must have been frequency tripled based on the metal cathode used is simply impinged on the cathode generating pulses of electrons [43]. Electrons are said to interact directly with atomic nuclei which then results in diffraction due to Coulomb interaction between the nuclei and the electrons in ultrafast electron diffraction. A high scattering power is also achievable with electron diffraction. X-rays on the other hand interact with electrons which may result in elastic scattering. X-rays have a small scattering cross-section with large penetration depth [42, 43]. See comparison between ultrafast electrons and x-rays as probes in Table 3.2.

Due to various advantages that have been reported on ultrashort electron pulses over x-ray

fluxes, researchers in the field have found it interesting to use the former in a femtosecond experiment. Such advantages include low intensity lasers, better atomic elastic scattering cross-sections, non-use of large scale accelerators etc. [43] and of course we can include health issues as well. Trade-offs between temporal resolution and space charge broadening need to be accounted for in either of these techniques as the former is limited by the latter. This can however, be compensated for by using an improved electron gun.

Comparison between x-rays and electrons as ultrafast probes are presented in Table 3.2.

	Electrons (50-500 kV)	X-rays (0.5 nm)
Ratio of inelastic/elastic scatering events	3	10
Energy deposited per single inelastic event	20 eV	8000 eV
Scattering cross section	1×10^{-18} cm^2	1×10^{-24}- 1×10^{-23} cm^2
Penetration depth	$\approx10^{-9}$ m	$\approx10^{-4}$ m
Focusing and manipulation	fairly easy	difficult
Spatial resolution	10^{-4} (in diffraction)	10^{-2} (in diffraction)
Challenges	space charging	photon fluxes

Table 3.2: Comparison of properties of electron and x-ray probes [42].

The next chapter describes the procedures involved in preparing ultra thin sample for ultrafast electron diffraction experiments.

4. Sample Preparation

In femtosecond electron diffraction (FED) like ours, very thin samples need be prepared for the diffraction experiment. This is because for a transmission diffraction geometry operating in the electron energy range of 30-50 keV, a sample thickness of tens of nanometres is required. In addition, the sample should have a good scattering cross-section and can be homogeneously photo-excited. Different methods are available for obtaining such thin samples. They include sputtering, focused ion beam, scotch tape and ultramicrotome. In our group, ultramicrotome has always been preferred and thus shall be discussed in detail in the following section. For detailed explanations of the remaining methods, refer to [9, 10] together with the references there in.

The ultimate goal when preparing a sample for ultramicrotoming is to be able to cut a sample that will be experimentally viable i.e., a good diffraction pattern should be obtainable from such a sample. This means that samples that are electron transparent are required. This may not always be the case however. In order to achieve an electron transparent sample, thicknesses of tens of nanometres (20-30 nm) are required, at least for my own kind of sample. Due to this requirement, one encounters difficult challenges. The ultramicrotome and its associated challenges are discussed below.

4.1 Ultramicrotome

Before we discuss this method, let us briefly highlight the processes involved in getting the sample ready for ultramicrotomy. We make use of resins for sample mounting (see Figure 4.1). It is a hardened material made out of epoxy and is prepared and supplied to us by the Central Analytical Facilities (CAF) here at Stellenbosch University. The hardness of the material is particularly good so that no deformation occurs for example when it is tightened in a sample holder. It also does not react with the sample. We possess bulk crystals of our sample about half a millimetre in sizes. Sometimes, there might be a need to first recut the crystal with a sharp razor blade to a manageable piece ($\sim$200 µm) that can be mounted on a resin. Whichever the case, usually we have a resin in a cone-like shape with a circular flat top. If the top is not flat, it first has to be flattened with sandpaper. A small drop of super glue is supplied to a clean surface (a plane sheet or a glass plate), after which the flat top

of the resin is then brought into contact with the glue, transferring some of the glue to the resin. It is then used to pick up the sample piece resting on another clean surface (a plane sheet or a glass plate). The sample piece can be positioned correctly with this method. This is one method. Another method though is to embed the sample piece within the resin. The sample is placed correctly in the resin box and the liquid resin is poured into the box. It (sample piece and resin) is then baked hard. The latter method is usually prepared at CAF since the resins are produced by them. Both methods are interchangeably used in our group depending on the nature of the sample. The former method is what is usually used for the 1*T*-$TiSe_2$. When the sample is nicely prepared in this manner, only then is it ready to be "ultramicrotomed". Figure 4.1 shows a sample mounted on resin.

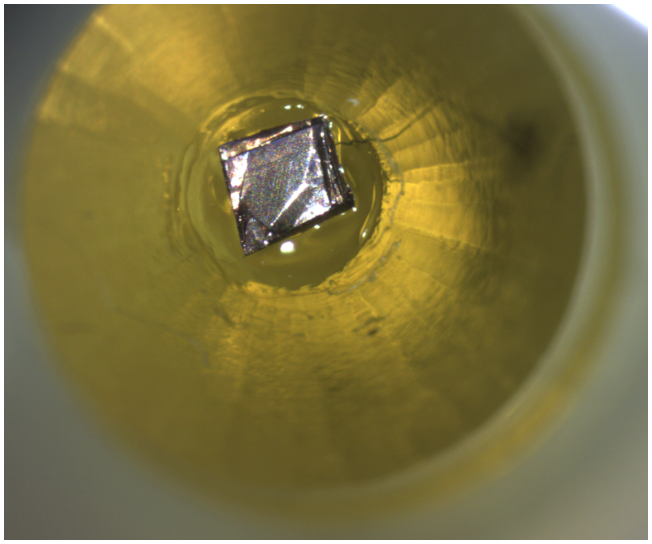

Figure 4.1: Sample mounted on a cone-like resin with the help of a glue.

The ultramicrotome that our group uses in cutting our samples is situated at CAF. Figure 4.2 shows the ultramicrotome with a diamond knife mounted together with the sample ready for cutting. The diamond knife belongs to our research group.

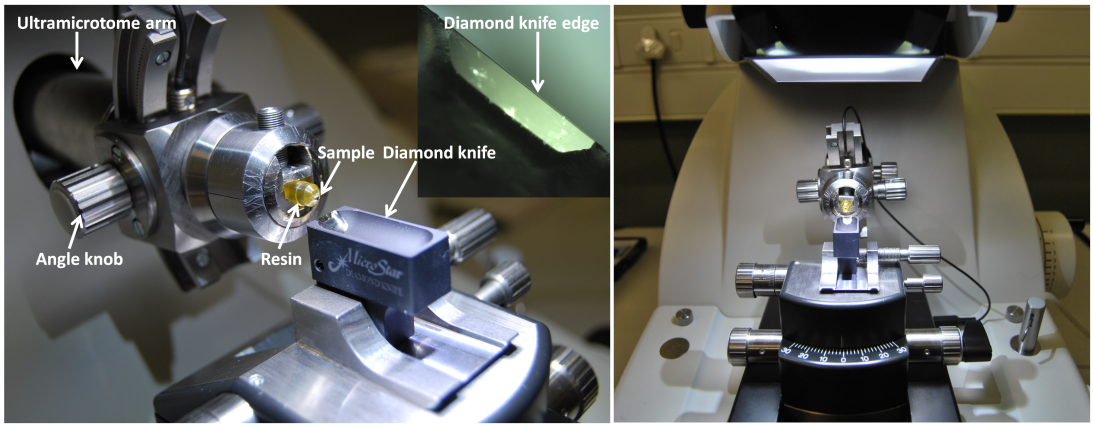

Figure 4.2: The Ultramicrotome at the Central Analytical Facilities (CAF) showing the mounted sample on a resin ready for ultramicrotoming. A diamond knife for preparing the ultra thin sample is positioned and aligned parallel to the surface of the sample. Once the alignment is complete, the boat-like shape of the diamond knife is filled with water so that cut samples float nicely on the water.

To cut a sample successfully with an ultramicrotome, an important tool is required - a diamond knife. Depending on the sample, a glass knife can also be used. We use the diamond knife to cut our sample. However, the glass knife can be used to prepare the surface by using it to get rid of some layers from the surface of the sample before using the diamond knife. Because of the fragile and expensive nature of the diamond knife, it is carefully and gently mounted on the ultramicrotome and the resin with the sample is aligned to the edge of the knife i.e., after preparing the surface of the sample with a glass knife. To align the sample, the microscope is focused on the knife-edge and the sample moved close such that the knife-edge's reflection is seen on the sample's surface. Proper angle adjustment (up-down and left-right angles) is made until the sample is parallel to the knife-edge in such a way that once the arm of the machine begins to move the space between the sample and the knife-edge remains constant. The boat-like shape to which the diamond knife is attached is then filled with water up to the edge of the knife avoiding any formation of meniscus. Parameters like the thickness of the sample, the arm speed as well as the step size (if done manually) to which the arm has to move closer to the knife edge can be specified. Thus, the arm moves the sample parallel to the knife edge cutting a thin slice off the sample. The arm moves down and up utilising the supplied information until another thin slice is cut from the sample surface. This process is repeated until enough pieces of the sample float on the surface of the water whereby the movement is stopped and the slices are collected. This process can either be automated on the machine or executed manually.

The transmission electron microscopy mesh, always shortened as a TEM mesh is used to collect the floating film. There are two types: a carbon mesh and a non-carbon mesh. The mesh (non-carbon) is lowered beneath the water surface using a tweezer and an eyelash attached to a toothpick is used to drive the sample onto the mesh in order not to touch the end of the diamond knife. It is lifted gently and carefully onto a filter paper to absorb any droplets from the mesh before being stored inside a sample box designed to hold meshes. If the mesh is not properly dried, the sample can be lost in the process of putting it into the sample box since there could be a water film and sample residing together in a given mesh hole. Such water film can pop up or smear the wall of the sample box if the mesh is not allowed to dry properly. A carbon mesh can also be used for sample collection. The carbon mesh has a thin layer of carbon on the mesh and can hold cut samples nicely. However, it has its own associated problem. The carbon film can absorb and scatter the electron beam thereby leading to background noise and may possibly obstruct the signal generated from the sample. Therefore, it is best to avoid the use of carbon meshes.

The challenges associated with the use of an ultramicrotome are good alignment and transferring of the floating films. For a non-reflective sample surface, it is often hard to achieve a good alignment between the sample and the knife edge. Because our sample is a layered compound, we usually minimize this challenge by cleaving the surface of the sample with a scotch tape. Refer to explanation on scotch tape by Haupt [10]. Figure 4.3 shows scotch-taped and non scotch-taped samples.

(a) 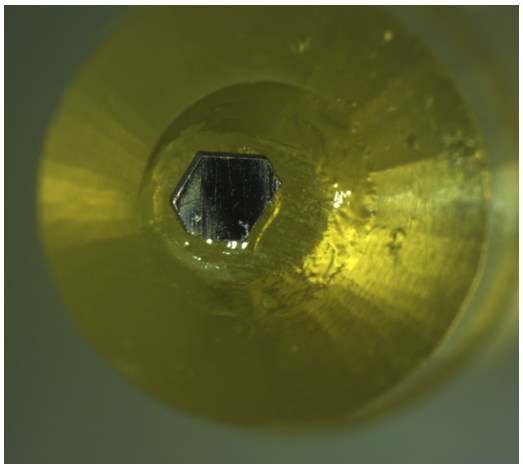 (b) 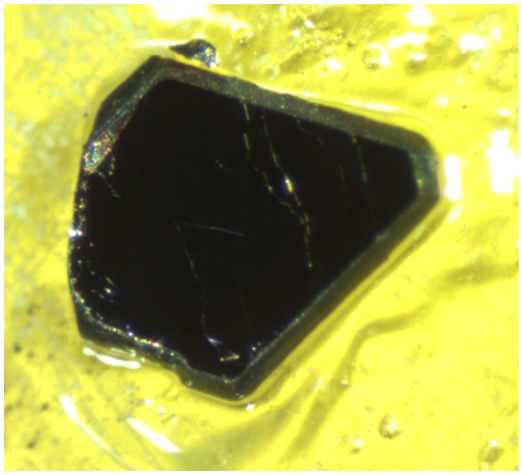

Figure 4.3: (a) Non scotch-taped sample. Sample like this is difficult to align with the knife edge for successful cutting. (b) Scotch-taped sample has a reflective surface onto which the knife-edge can be aligned and cutting is thus made easier.

Once the reflective surface is nicely revealed, the image of the knife edge can then be seen on the sample surface aiding a better alignment. Another such challenge is picking the thin slices (or floating film) from the water surface. Without a steady hand and patience, all the thin slices can be lost. We found in a manual [44] that a loop can pick up the sample nicely from the water surface. This has been tested and was quite an improvement.

4.2 Preparing an experimentally viable sample

A successful good sample should be homogeneous and fill at least three quarter of the mesh hole. This can only be identified under the microscope. Once such a good sample is obtained, it is then mounted on the sample mount. First, an aperture 100 µm in diameter is glued centrally onto the sample mount with silver paint. The mesh hole containing the good sample is positioned on the aperture and then glued to the aperture with the same silver paint. This procedure requires a steady hand, concentration and patience and it is done under the microscope. See Figure 4.4 for example.

(a) 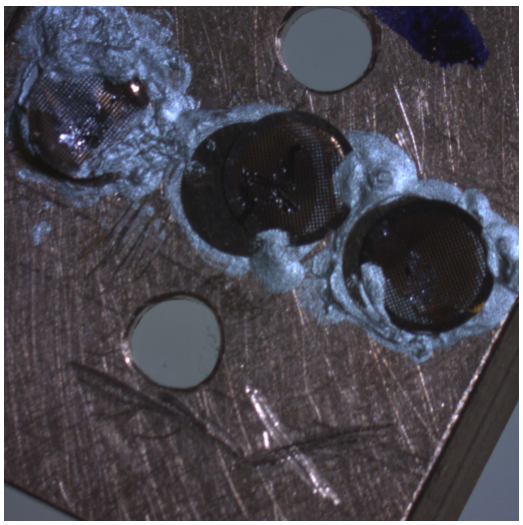 (b) 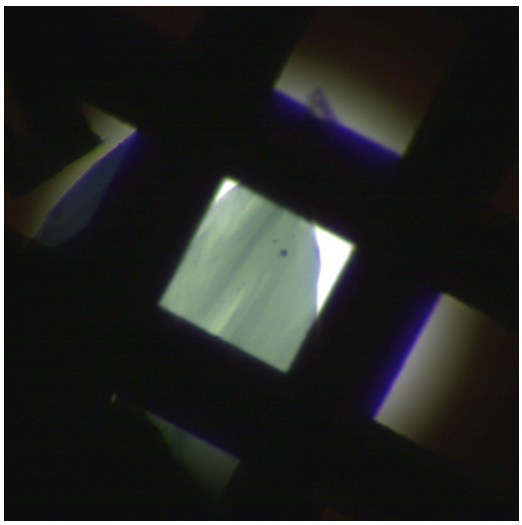

Figure 4.4: (a) Mesh on aperture mounted on the sample mount. This is transferred into the chamber where measurement is then performed. (b) Closer view of a 30 nm sample sitting on a mesh size of 85 µm placed onto an 100 µm aperture.

A sample prepared with an aperture has the advantage of reducing the background signal immensely improving the diffraction signal. This is because only the sample surface area has been exposed to the electron beam with the aperture blocking all other parts of the mesh, filtering the UV pulse coming through into the chamber together with the electrons.

5. Measurement and Analysis of Data

5.1 Stability of Electron Beam

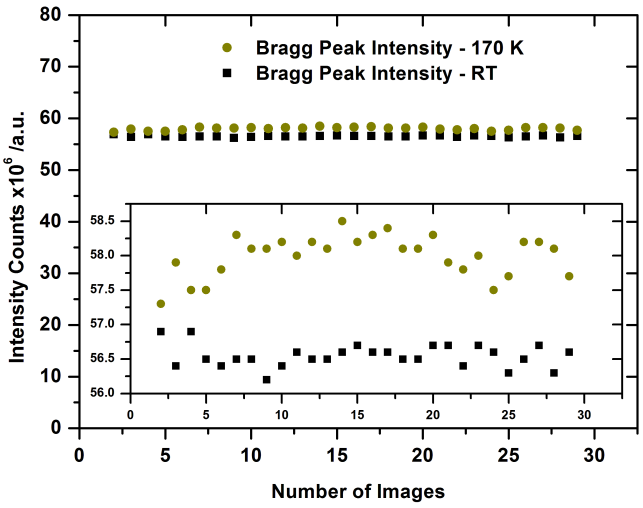

Figure 5.1: Graph showing the stability of the electron beam for half an hour of acquired images. It shows no considerable fluctuations even after waiting for almost two hours to acquire the same number of images. This shows how stable the laser beam is.

There are major considerations to be taken account of before running any kind of electron diffraction measurement with short electron pulses - be it a steady-state or time-resolved. The steady-state here means that the sample is not subjected to an optical pump pulse, and only the electron probe pulse is used. Those major considerations include the stability of the laser output, good alignment of the beams (pump and probe electron beams), the electron number per pulse together with its pulse duration at the sample, the transverse coherence length and other miscellaneous precautions.

To know how stable our electron beam is, we normally take a few tens of images of our sample and then look by how much the intensity has dropped over time. For example in Figure 5.1, we have acquired thirty images and since each image takes around a minute to be acquired it means that about half an hour was spent in acquiring the images. The error in the intensity counts over the said duration for the room temperature (RT) data is $\pm 0.2\,\%$. Almost the same stability is achieved for a sample cooled to 170 K. In this case, an error in the intensity counts is calculated to be $\pm 0.3\,\%$ after almost two hours of cooling. This means that the stability of our beam is adequate for our experiment. Temperature shouldn't play a role in how stable the electron beam is. It merely demonstrates that after almost two hours of cooling, the laser was still stable. A point to note is that the stability of the electrons is not only dependent on the laser source but also on our cathode gold layer. To achieve this kind of stability also translates to the fact that our cathode gold layer does not degrade easily.

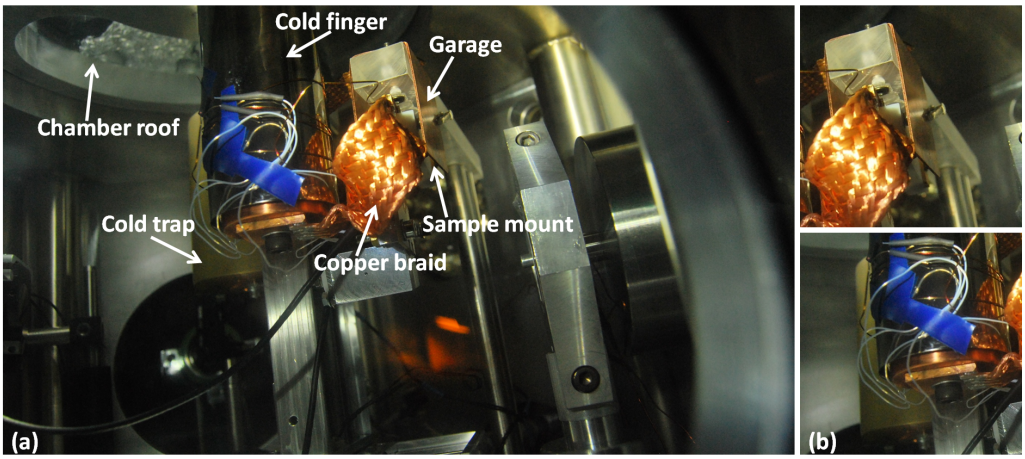

Figure 5.2: (a) A cold trap that takes in liquid nitrogen is connected to a garage that houses the sample used for cooling to a low temperature. The liquid nitrogen freezes out any water molecules in the chamber. (b) Shows the 'zoom in' of the garage with the sample residing in it (top) and the cold trap together with the cold finger of the cryostat.

5.2 Cooling

Since our sample undergoes a phase transition at ∼200 K or below 200 K, it is necessary to cool down the sample to the temperature where a phase transition can be observed. Therefore, we use a closed cycle cryostat or cryogenic refrigerator which has an expander DE-204AF with a DMX-20 interface. The interface has an operating temperature range of <8 K to 355 K and sits inside the chamber so that, together with the expander, a sample can be cooled down to 9 K or less. A copper braid is attached to the cold finger of the interface which thermally couples the cryostat to the sample. A sensor cable from the cryostat is also attached to the sample mount which is the white cable seen wound around the cold finger in Figure 5.2 and this is connected to a temperature controller. The expander has no mechanical contact with the interface but rather is separated by isolation bellows that isolates the interface from any form of vibration and is itself connected to a compressor.

Depending on some factors such as the growth conditions of a crystal, a sample may have to be cooled down to far below the phase transition temperature to see the signature of charge density waves (CDWs). For this sample, it is uncertain why sometimes one needs to cool down far below the phase transition temperature to see the CDWs. Nonetheless, going too low in temperature implies that we run a risk of condensation on the sample. Once this happens, the consequence is that we have a reduced signal from our sample due to water vapour molecules that stick to the surface of the sample. The impingement rate of these molecules which is the number of these molecules that are incident upon a unit surface area per unit time is calculated to be $1.96\times10^{16}\,\mathrm{cm}^{-2}\mathrm{s}^{-1}$ for a vacuum pressure of 10^{-6} mbar and because two molecules can collide, we therefore calculated for the volume collision rate to be $7.12\times10^{30}\,\mathrm{cm}^{-3}\mathrm{s}^{-1}$. Since collision of two of these molecules account for one impingement.

In order to overcome the condensation problem, we usually pre-cool with liquid nitrogen to freeze out any water vapour molecules that could perhaps condense on our sample. The connection of the cold trap is made to a garage where the sample is normally "parked"

whilst cooling down. This means that the sample has no direct view of main vacuum chamber so that in this state no ballistic molecules reach the sample but first stick to the surface of the garage hanging over the sample and then freezes out. This is because the garage itself is cold. The only time the sample has a direct view of the chamber is when measurements are taken. For example, we may move the sample out of the garage when we have to take a measurement and may remain out of the garage for longer if a scan needs to be performed at a low temperature especially during a transient measurement. The pre-cool with liquid nitrogen reduces the problem of condensation significantly thereby preventing a degraded signal when cooling the sample. Figure 5.2 shows the sample residing in the garage.

Transient Measurement

Because we would want to resolve structural dynamics on the atomic scale, it means that transient measurements are required in ultrafast electron diffraction. There is a delay between the pump and the probe (electron) pulse which is adjustable in order for both pulses to temporally overlap. In order words a time zero needs be achieved. Before determining time zero however, as we mentioned earlier, there is a need to first check the pulse duration of the electron beam since it determines the temporal resolution of the experiment.

Pulse duration

A knowledge about our pulse duration is always critical in our setup since we would like to know what our temporal resolution is for a particular experiment, even though we do not expect this to change overtime. To determine the duration, different methods are being used. This includes the interaction of electron pulse with a short-pulsed laser where the electrons are scattered off a ponderomotive potential established by the short laser. Refer to [9] and the references there in. In our group, a streak camera [45] developed over the years has always been very effective in determining our pulse duration. The technique of our streak camera requires the interaction of an electron pulse not with a pulsed laser but with a gradient electric field in time $\frac{dE}{dt}$ created due to laser interaction with a photo-switch. The photo-switch short circuits the streaking plates. Also, instead of the electrons scattering off a potential, what determines the pulse duration in the case of the streak camera is by measuring the streaking length and the streaking velocity of the deflected beam. This deflected electron beam is seen as a streak on the detector. Figure 5.3 shows the unstreaked and streaked electron beam. The operating principle has been described at length in [45]. A

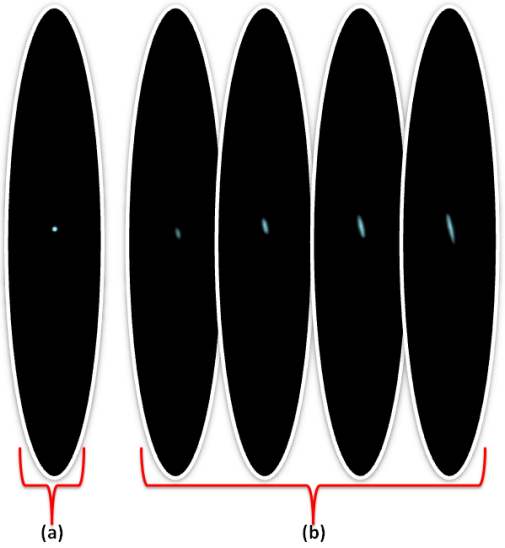

Figure 5.3: Unstreaked and streaked electron beam is seen on the detector upon passing through two streaking plates of the streak camera with rapidly changing electric field. The unstreaked beam (a) is when the voltage on the streaking plates is switched off and contains $8000e^-$. The streaked beam (b) contains $1000e^-$, $2000e^-$, $4000e^-$, and $8000e^-$ and respectively has a pulse duration of 1.10 ps, 1.54 ps, 1.92 ps and 2.43 ps.

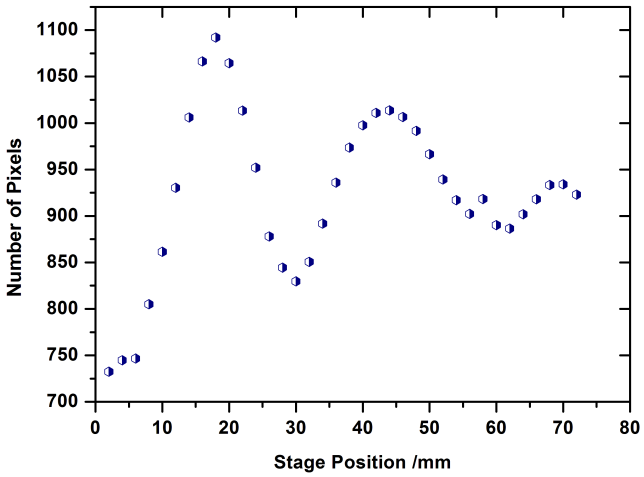

Figure 5.4: Mapped-out oscillation in the streaking plates after a 50 mW pump laser illuminates the GaAs. The electron beam on their arrival in the streaking plates gets deflected and the deflection is measured as a position on the detector.

voltage of 600 V is applied across the streaking plates and the laser pulse irradiates the GaAs photo-switch initiating the electric field oscillation since the plates act as a RLC circuit. The mapped-out oscillation of the electric field as the electrons pass through the streaking plates is shown in Figure 5.4 in terms of the position of the deflected beam on the detector and the stage position. With this principle, we have also measured our pulse duration for various electron numbers per pulse and obtained pulse durations that are quite close to previous measurements. A pulse duration of 1.10 ps for an electron number of 1000 per pulse was obtained. Pulse durations of 1.54 ps, 1.92 ps and 2.43 ps were respectively obtained for electron numbers of 2000, 4000 and 8000. We operated at 5000 electrons per pulse to ensure that the strength of the signal from our sample is increased significantly, knowing of course that we run the risk of losing a good temporal resolution. Such a high number of electrons per pulse is necessary because sometimes the sample might be a bit too thick to obtain a strong signal.

Figure 5.5 displays the electric field as a function of the trigger-pulse delay. Meaning that the position of the deflected beam on the detector as seen in Figure 5.4 has been transformed into electric field and the stage position converted to the trigger-pulse delay. The gradient electric field $\frac{dE}{dt}$ has been calculated to be 3.6×10^{17} V/m.s and is indicated on the figure.

With the same streak camera, we can easily determine our time zero. Unlike in the case of the pulse duration measurement where the voltage applied across the streaking plates is 600 V, this high voltage is not required when determining time zero as only 50-60 V is enough with a pump power of 50 mW - same pump power as was used for the pulse duration measurements. We then optimise the trigger-pulse delay for the photo-switch by moving the stage in a small step-size. The point just where the electron beam starts oscillating is our time-zero and this is noted. This time zero is the position just where the electron beam sees the highest electric field gradient. Figure 5.5 shows the amplitude of the electric field as a function of the trigger-pulse delay time which is obtained by converting Figure 5.4. Once the time zero is established, the transient measurement is then ready to be performed. See Appendix A.5

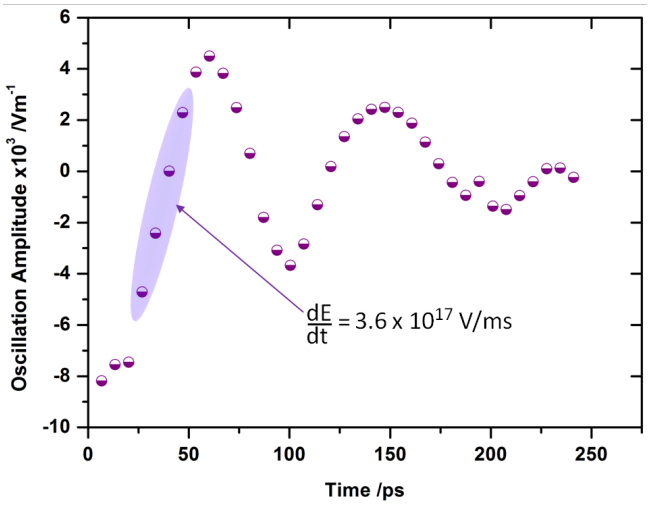

Figure 5.5: The amplitude of the electric field is plotted as a function of the trigger-pulse delay. The elliptical shade shows the gradient of the electric field which has been calculated to be 3.6×10^{17} V/m.s. This is a temporal field gradient that is large enough and with good enough strength that can create a large deflection to create a streak on the detector.

Figure A.2 for the streak camera used.

5.3 Fluence

A crucial parameter to be determined once a transient measurement is ready to be performed is the pump fluence at which the sample can be excited. To determine this, a programme has been designed by our research group in LabView to automatically communicate with a FireWire 400 Monochrome Industrial Camera (DMK21BF04). What the programme does is to read in the camera parameters and then calculate the full width at half maximum (FWHM) area in μm^2 from which the fluence can be calculated if the pulse energy is known. Therefore, a power metre measures the pump power of the laser and this is adjusted accordingly on the programme to be sure that a correct pump fluence (Energy [mJ]/Area [cm^2]) is set. Of course this is important as the structural dynamics of the sample can only be observed after cooling to a low temperature by giving a certain energy to the sample and analysing the response of the low temperature features appropriately. Not only that, given that to obtain very thin samples on the order of 20-30 nm is challenging, destroying a good sample by improper calibration of the fluence will not be a good idea. Figure 5.6 shows the pump beam profile obtained from the camera for different FWHM.

To effectively and accurately determine our fluence, we have decided to measure the beam diameter before the lens that focuses the pump beam to the target in order that we have an idea what our beam waist diameter is. The beam profile at the target after the lens (i.e., in focus) has also been determined.

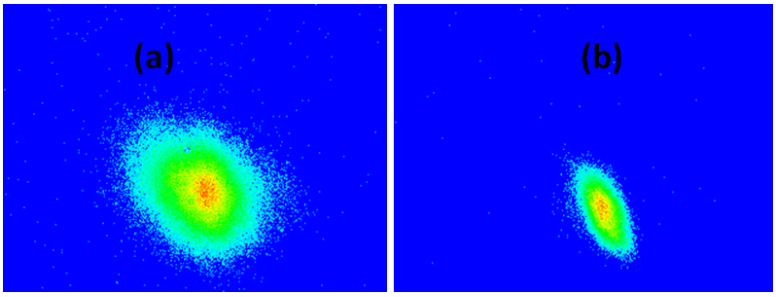

Figure 5.6: The FireWire 400 CCD Mono camera communicates with a LabView programme. The programme reads out the camera's data and by calculating the FWHM area, the appropriate pump power of the laser can then be set. (a) Shows a pump beam with a large FWHM diameter of 384 µm that is not in focus. (b) Shows a pump beam with a small FWHM of 211 µm as the beam gets closer to focus.

Laser Beam Parameters

For effective performance of laser, there is a need to understand some of its crucial parameters besides for example the output power or pulse energy. Such parameters include beam diameter, spatial intensity profile, divergence etc. A better understanding of these parameters lead to better results. Because all other parameters are usually taken care of when the laser system is serviced, we shall therefore be looking at only the beam diameter as this is crucial in characterising our fluence appropriately and accurately before measurements.

Beam waist diameter is one of the important attributes of a laser beam defined as twice its beam radius or the full width at half-maximum (FWHM) diameter. Since we illuminate our sample during a time-resolved measurement, understanding quantitatively how much fluence is required for a specific kind of sample implies understanding what the beam diameter (diameter illuminated on the lens) is at full power before the lens that focuses the beam to the target sample and the beam profile at the target sample. First, we show the measurement of the beam diameter before the lens.

We have used a knife-edge mounted on a stage and driven into the laser path in small steps. The result is that the data acquired by driving the knife-edge into the beam path is an integrated measurement from which the beam diameter can be retrieved and thus ultimately what our beam waist diameter is before focusing i.e., before the lens. Shown in Figure 5.7 (a) is the normalised integrated power as a function of the stage position together with an error function fitted to the data.

The error function (i.e., the fit function) is known to have a Gaussian function as a derivative and hence the derivative of the function fitted to the data produces a Gaussian profile which actually represents the beam profile (see Figure 5.7 (b)). The FWHM of the beam profile is $\sim$2.8 mm and this is the beam diameter on the lens. The FWHM can be derived from the Gaussian function and is given by $\frac{2\sqrt{\ln 2}}{b}$. With $b = 0.5858$, this also gives $\sim$2.8 mm. This is the beam diameter before the lens meaning that a theoretical prediction of the beam waist diameter $2w_0$ together with the Rayleigh range X_R can be estimated by using the following equations:

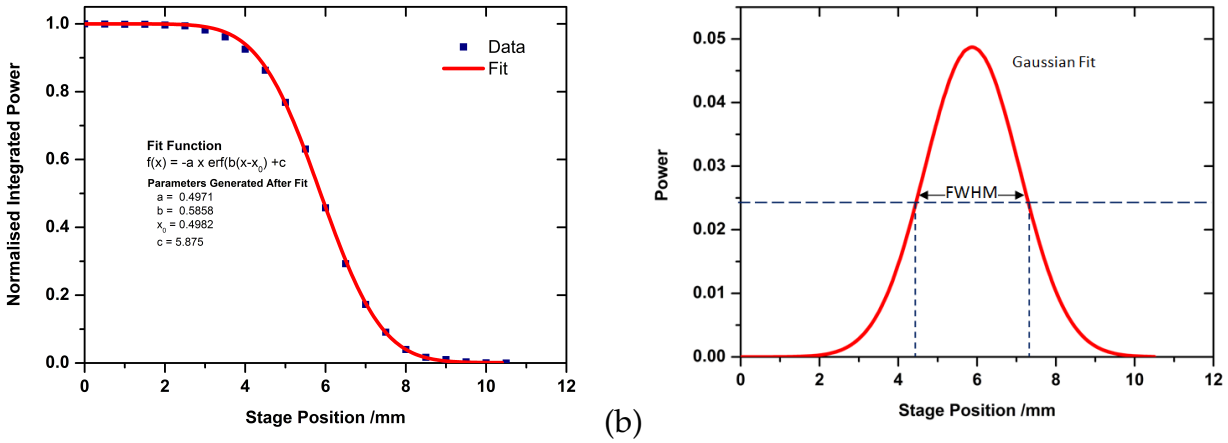

Figure 5.7: (a) Graph showing measurement of laser power as a function of stage position which has been obtained using a knife-edge method (blue square dot). An error function which is an integration of a Gaussian function has been fitted to the data points (solid red line). (b) The Gaussian profile has been obtained through differentiation of the fit function that incorporates the data points and the FHWM diameter of the beam obtained as ∼2.8 mm.

$$2w_0 = \left(\frac{4\lambda}{\pi}\right)\left(\frac{F}{D}\right)$$

$$X_R = \frac{\pi w_0^2}{\lambda},$$

where D is the beam diameter before the lens, F is the focal length of the lens, w_0 is the beam waist radius and λ is the wavelength of the laser being measured.

With $F = 100$ cm, $D = 2.8$ mm and $\lambda = 775$ nm the beam waist diameter $2w_0$ together with the Rayleigh range X_R were estimated to be ∼352 µm and ∼126 mm respectively.

Now, we present how the FWHM diameter after the lens can be measured. Figure 5.8 shows the setup for the measurement in focus. The beam is incident on a lens of focal length 100 cm which focuses it onto the sample sitting in the chamber. Since it is difficult to precisely measure the profile of the beam at the sample, we therefore measure it outside of the chamber. With the help of the window of the chamber the beam is reflected off the window and is directed with some optics (not shown in the figure) onto a camera with a filter in the path to the camera to avoid saturation.

To measure the FWHM diameter with this setup however is not trivial. The camera communicates with a LabView programme from which the image of the beam can be saved. So by moving the camera on a stage, the corresponding distribution of the beam profile is seen on the camera. This is thus analysed to retrieve the FWHM diameter of the beam. Figure 5.9 shows the plotted data.

The beam waist diameter has been determined to be ∼340 µm in focus at a distance of 1065 mm from the lens. Knowing this helps us to manipulate the beam profile on our sample and to accurately determine the fluence with which the sample is pumped. With this spot size or beam waist diameter, the beam diameter (diameter after lens is illuminated) D in focus and the Rayleigh range X_R can be calculated using the same equation as above.

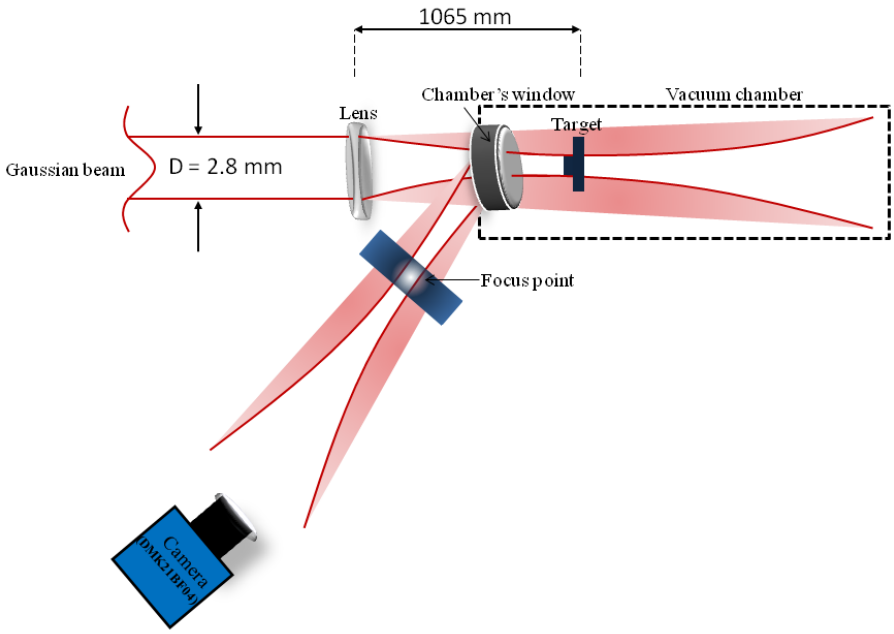

Figure 5.8: Pump beam setup in the UED laboratory showing how the FWHM diameter can be measured. The laser beam (Gaussian beam) is incident on the lens (100 cm focal length), the lens focuses the beam onto the sample and part of the beam gets reflected off the window of the chamber and this is directed onto the FireWire CCD Mono camera. The position of the camera can be varied with each position corresponding to a specific beam distribution on the camera. This can be saved and the diameter retrieved. Note that the focus point highlighted outside of the chamber is the same focus inside the chamber where the target sits.

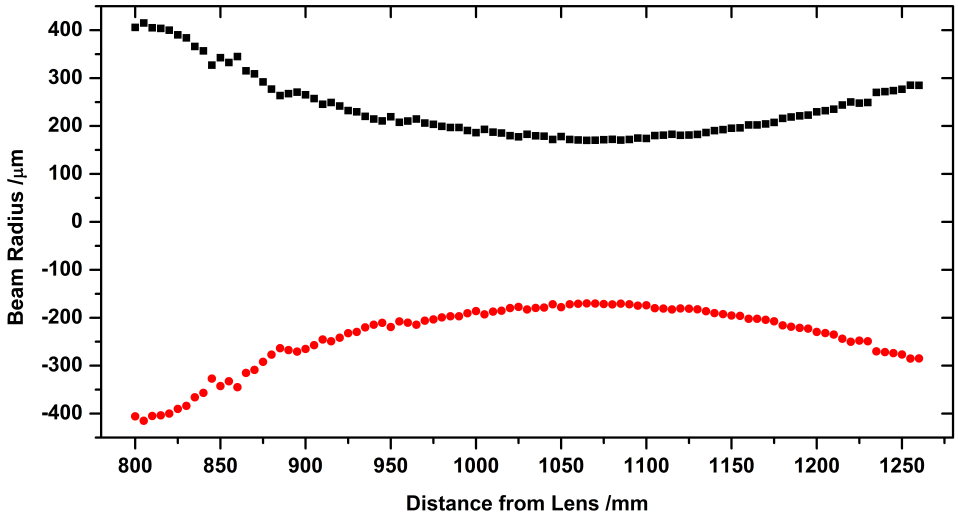

Figure 5.9: Graph showing the Gaussian beam width as a function of the distance along the beam. The beam waist radius and the corresponding beam waist diameter of the beam can be determined. The nominal focal length of the lens used is 100 cm.

The beam diameter D was determined to be $\sim$2.9 mm after the lens (at the focus) and the Rayleigh range to be $\sim$117 mm. Other parameters regarding the measurement can be estimated by using the model in Figure 5.10. Also see Appendix A.2.

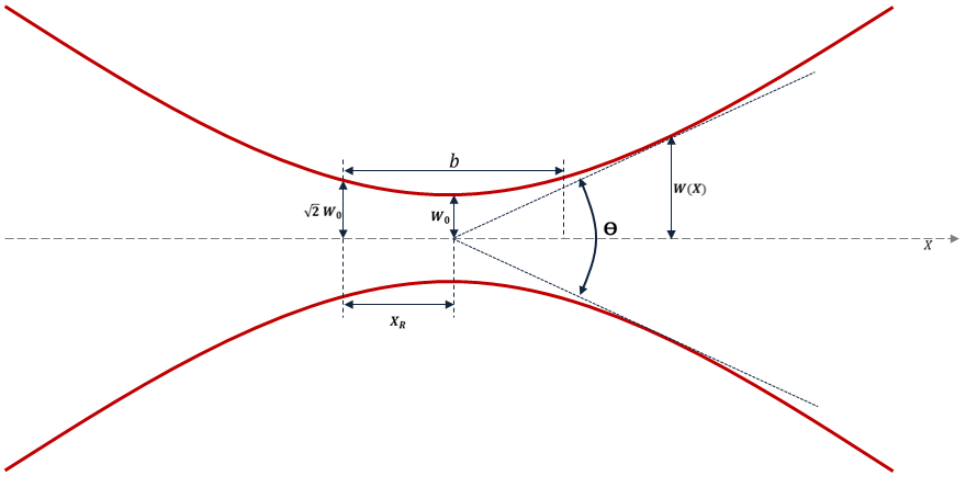

Figure 5.10: Sketch showing the Gaussian beam width w(x) as a function of the distance x along the beam. Θ is the total angular spread and b depth of focus. Other parameters are as defined in the above equations. See Appendix A.2 for equations/or definitions of other beam parameters.

5.4 Diffraction Data Analysis

There are different LabView programmes designed to either acquire data or aid in their analysis. One such programmes used in acquiring transient data is the UEDscan. Before acquiring any transient data with the programme, parameters such as the step-size, the stage position at time zero, number of scans to be taken etc. have to be specified. Once these parameters are specified, the programme is run by acquiring pumped and unpumped images which saves automatically to a folder with the date that the measurement is being conducted. This makes analysis easier as data can be accessed without confusion.

Now, to obtain any result is to first analyse the data acquired through measurement. In order to do this, there are different sets of designed programmes based on LabView to aid in the analysis. Depending on what aspect of the data one would like to look at, there is a corresponding programme to use. For instance, if we take a transient data as an example, there is a programme called DiffractionAnalysis which can be modified to fit the nature of the diffraction spots. Since diffraction spots bearing signatures of a hexagonal structure of transition metal dichalcogenides have been analysed in the past with this programme, it was easily adaptable to my own diffraction spots as they also bear hexagonal signatures. For this kind of transient data analysis, the programme takes in parameters like the step-size and the appropriate box size around the diffraction spot one wants to look at. It therefore analyses the pumped and the unpumped images by retrieving the Bragg and the CDW signals in terms of intensity change if both are specified for analysis. Such signals give you an idea about the evolution of the structures in time. Figure 5.11 (a) shows one set of diffracted spots specified for the programme.

As shown already in Chapter 2, at a low temperature phase, each Bragg peak is surrounded by six CDW (superstructure) peaks meaning that for every two Bragg peaks there is a CDW peak in between them. This means that the programme selects appropriately the various

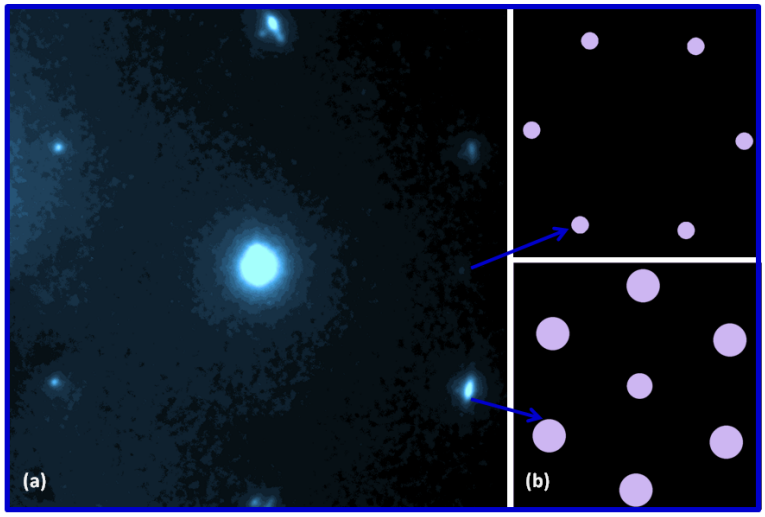

Figure 5.11: (a) shows the specified Bragg spots as well as CDW spots for a programme written in LabView to analyse. (b) Shows the automatic generation of the specified spots after analysis. The upper panel shows the CDW spots and the lower panel shows the Bragg spots.

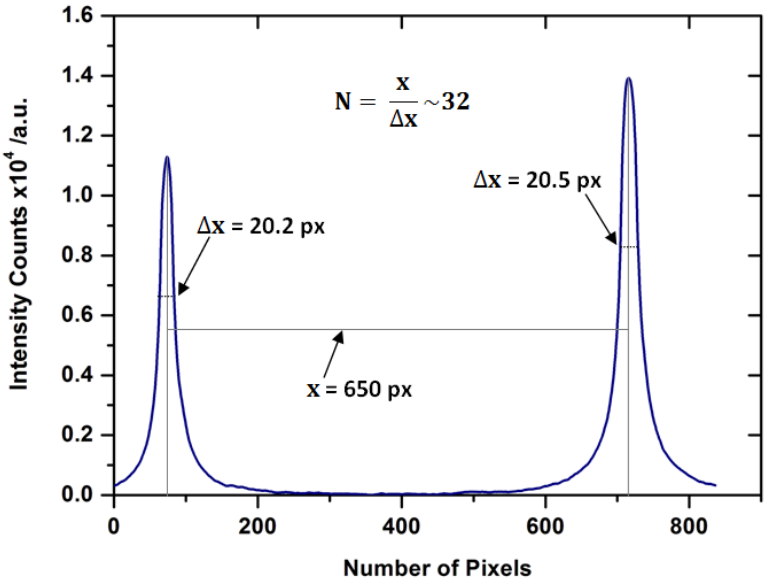

Figure 5.12: Two selected Bragg spots show the intensity distribution of the peaks from which the transverse coherence length of the beam is calculated for the 1*T*-$TiSe_2$.

CDW peaks and the Bragg peaks. Figure 5.11 (a) shows the experimental peaks the programme is commanded to select and (b) shows the various peaks that have been selected by the programme which is automatically generated during analysis. Note that the centre Bragg spot has six CDW peaks around it - not visible though in (a). Also see Chapter 6 Figure 6.5.

Transverse Coherence Length

Because the sample of study exhibits new features with larger periodicity than the crystal structure, it is essential that one has a good coherence length of the electron beam to reveal the structure of the crystal together with the new features (i.e., the CDWs). Hence, the impor-

tance of coherence length. Though this has previously been measured for various samples that have been investigated in our group, it is notwithstanding as the coherence of the beam for this particular crystal should still be determined. Another reason why it is necessary to determine it for our own measurement is that the transverse coherence length is dependent on the emission source size which in our case is the UV spot size on the photo-cathode. See for example Figure 3.3. This should not change until a user optimises the spot by adjusting the UV lens which of course was done in our measurement.

The transverse coherence length of the beam can be determined for a given crystal using a multiple slit grating approach as shown in [9]. This is because the number of scattering planes of a crystal is determined by the ratio of the distance between two diffraction peaks and the FWHM of the peaks. Thus, in a multiple slit grating, the N in Figure 5.12 will denote the number of slits given by $\mathrm{N} = \frac{\mathrm{x}}{\Delta \mathrm{x}}$ where x and Δx will denote the distance between the main maxima and the FWHM of maxima respectively. Following the same method as in a multiple slit, the coherence of the beam from the measurement of $1T$-$TiSe_2$ is calculated to be $\sim$11.3 nm from Figure 5.12. In our case, the N determines the number of scattering planes of the crystal instead of slits and this is multiplied by the appropriate crystal lattice constant which gives the transverse coherence length of the beam: $\mathrm{N} \times \mathrm{a} = \frac{\mathrm{x}}{\Delta \mathrm{x}} \times a$ where x and Δx denote the distance between two diffracted spots and the FWHM of the diffracted spots. The appropriate lattice constant of $1T$-$TiSe_2$ for this purpose is given by a = 3.54 Å and the peaks in the graph have been analysed from the generated experimental diffraction pattern of the sample.

6. Results and Discussions

In this chapter, we shall compare the room and low temperature simulated electron diffraction patterns of the 1T-$TiSe_2$ qualitatively with experimental electron diffraction patterns. Transient experimental data including the Debye-Waller effect and charge density waves will also be presented. First, let us qualitatively look at the simulated electron diffraction patterns and temperature dependent static experimental diffraction data obtained. Also note that all experimental data presented in Section 6.2, 6.3, 6.5, 6.6 and 6.9 are steady-state measurements which means that no optical pump pulse was used.

6.1 Simulation

A software programme known as Simulation and Analysis of Electron Diffraction (SAED) [5] is used in our group for simulating electron diffraction patterns of any sample provided that one has the structural refinement data such as the lattice parameters, space group and the atomic coordinates of atoms making up the unit cell of such a sample.

6.2 Room Temperature Electron Diffraction Pattern: Simulation and Experiment

Structural refinement data obtained in terms of the atomic coordinates of the atoms making up the unit cell of 1T-$TiSe_2$ together with the lattice parameters as well as it's space group at room temperature have been obtained from [6, 16, 19] - refer to Section 2.2 for the lattice parameters. With this information, it is straight forward to obtain a room temperature simulated electron diffraction pattern of the crystal along the [001] Laue zone showing, as has been learnt from literature ([1]) and in good agreement with our experiment, the signature of the hexagonal structure of the crystal. This is shown in Figure 6.1 (b). Figure 6.1 (c) shows our experimental pattern and Figure 6.1 (a) shows the real-space unit cells of the crystal in the normal phase i.e., at room temperature. The dark spots in the simulation and the white spots in the experiment are the generated Bragg spots because the sample satisfies the Bragg condition i.e., $\sin\theta = n\lambda/2d$.

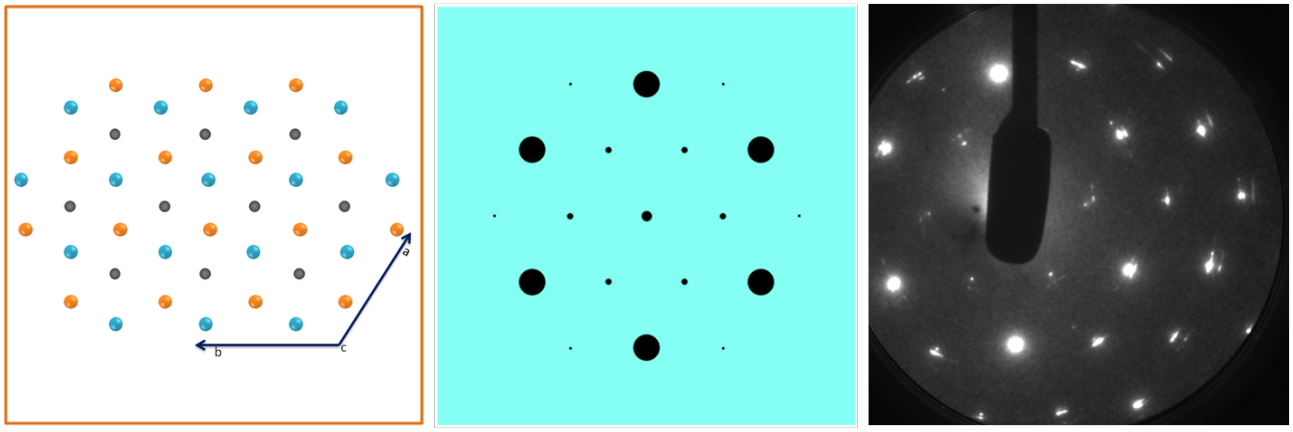

Figure 6.1: (a) A schematic representation of the real-space unit cells of the undistorted phase with the blue, orange and grey colours denoting the selenium upper layer, selenium lower layer and the titanium layer respectively. (b) Simulation showing the electron diffraction pattern at room temperature. The room temperature parameters are fed into the software and sample thickness of 30 nm and a high voltage of 30 kV are specified. The hexagonal structure of the crystal shows a strong signature in the generated pattern. The black spots are the Bragg spots with the bigger spots indicating an constructive interference resulting from where the electron density distribution is highest in the crystal. (c) Electron diffraction pattern of 1*T*-$TiSe_2$ obtained from a measurement at room temperature and at 30 kV for a 30 nm thick sample. The white spots are the equivalent of the black spots in (b) which are also the Bragg spots. More higher orders are however seen compared to that obtained from the simulated pattern.

The simulation has been performed for a 30 nm thick sample with the electrons accelerated with 30 kV. A scenario created to correspond to our experimental conditions except that we deal in the case of the simulation with a perfect sample and a perfect beam. It should be noted that more higher orders are seen for the room temperature (RT) diffraction pattern of the experiment in contrast to the simulated diffraction patterns. The reason for this however is not clear. Nonetheless, we observed that only a thickness on the order of 15 nm or less could produce higher orders at 30 kV similar to those of the experiment. This does not necessarily mean that the thickness of our sample is within that range as such a thin layer is difficult to achieve in practice. Refer to Table A.1 for the atomic positions used for the simulation at room temperature.

Comparison

Because not much information is retrievable from the room temperature patterns of the simulation and experiment by merely comparing the distributed Bragg spots by eye, we have decided to qualitatively compare these two. Such a comparison is shown in Figure 6.3. The orders that have been plotted in Figure 6.3 (a), (b) and (c) have been respectively depicted in Figure 6.2 with the green colour representing the zero order, blue for first order, cyan for second order and orange for third order both for simulation and experiment.

By looking at the indexed peaks in Figure 6.3 note that there are peaks seen in a particular Bragg order reflections in the experiment that might not be seen in the simulation and vice versa. Again why this is so cannot be easily established. For example in Figure 6.3 (a) a peak order of (300) is seen in the experiment but not in the simulation and a peak order of (-100) in the simulation but absent in the experiment. (3-10) and (3-20) are seen in experiment but absent in the simulation respectively for (b) and (c). The peaks that have been plotted for the case of simulation only indicate that the area is proportional to the intensity. Note that the

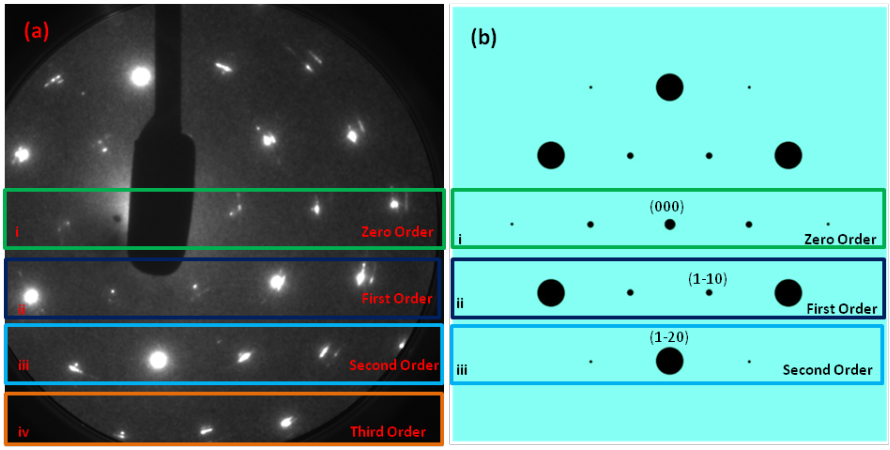

Figure 6.2: (a)i and (b)i show the zero order Bragg reflections, (a)ii and (b)ii show the first order Bragg reflections, (a)iii and (b)iii show the second order Bragg reflections and (a)iv shows the third order Bragg reflections which is the higher order absent in (b). These are for the experiment and the simulation at room temperature respectively.

third order for the experiment is not plotted because there is no third order in the simulation to compare it with.

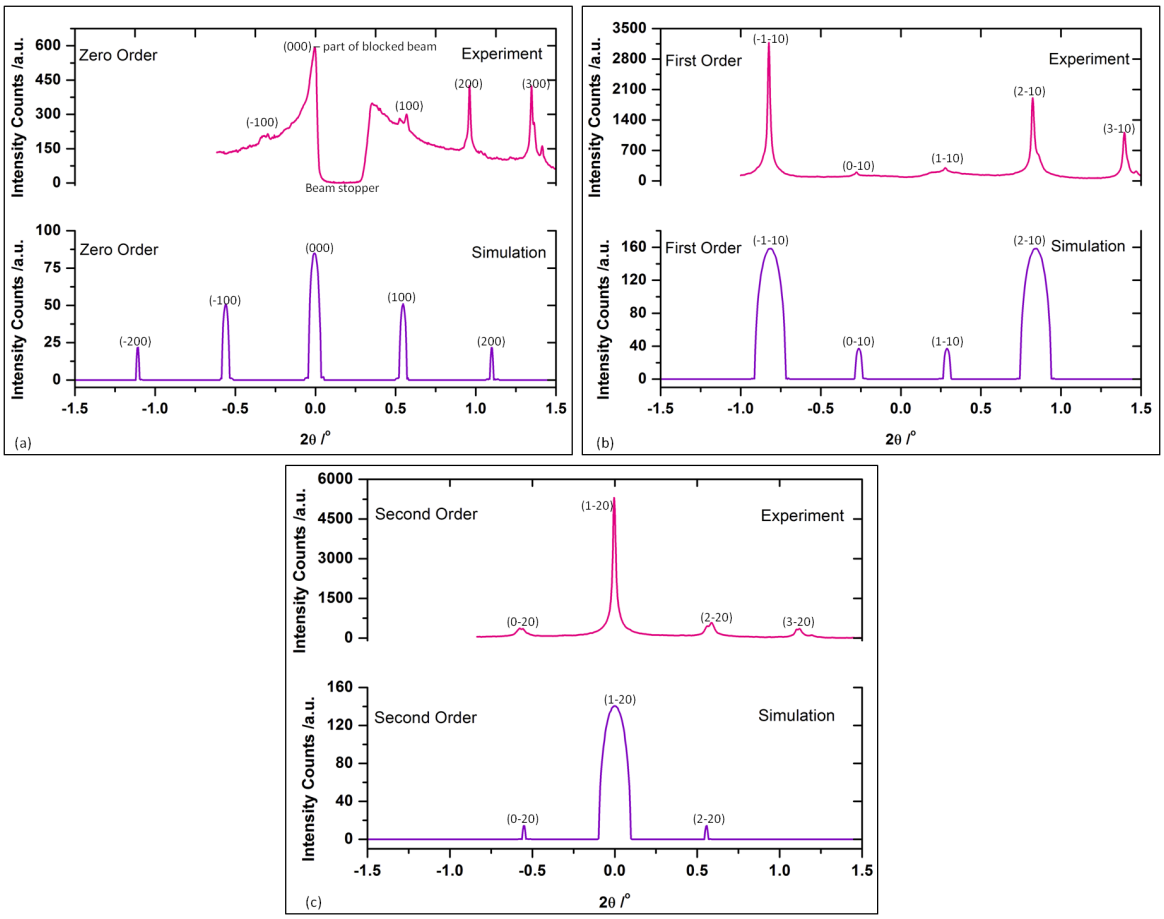

Figure 6.3: (a) A plot of Figure 6.2 (a)i and (b)i as a function 2θ showing the variation in the intensity distribution of the peaks. (b) A plot of Figure 6.2 (a)ii and (b)ii as a function 2θ showing the variation in the intensity distribution of the peaks. (c) A plot of Figure 6.2 (a)iii and (b)iii as a function 2θ showing the variation in the intensity distribution of the peaks. The graphs are for the room temperature or undistorted phase.

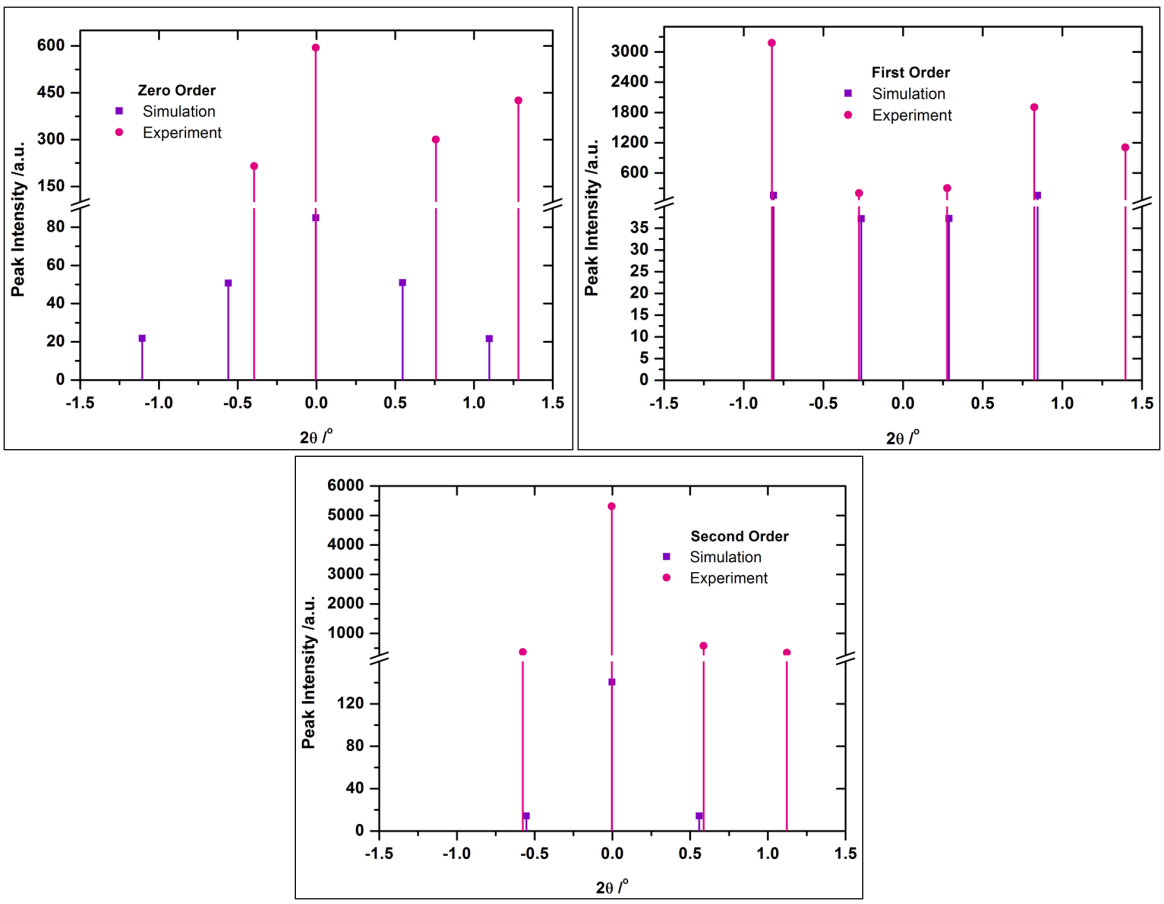

Figure 6.4: The peak intensities for Figure 6.3 have been plotted as a function of 2θ clearly showing the difference in intensities between the simulation and the experiment. This has been plotted for all the Bragg order reflections.

6.3 Low Temperature Electron Diffraction Pattern: Simulation and Experiment

Whilst the room temperature pattern of the simulation has been interesting so far, what is even more interesting is the idea of being able to generate an electron diffraction pattern of the sample at the low temperature phase by simulation. This is because in this phase, superstructures characterising the sample have been widely reported experimentally - features we are very much interested in. With the same SAED software and with the same requirements as in the case of the room temperature simulated pattern, the electron diffraction pattern for the low temperature structure was obtained. The difference between the room and low temperature structure however is that there is now a change in crystal symmetry as well as a double of lattice parameters (2a, 2b and 2c) as the crystal undergoes a phase transition at a low temperature and these parameters have been obtained from [6, 16, 19]. Most importantly, the displacements of the atoms as the sample undergoes this transition has to be known. This information was given in [1]. The titanium atoms are said to be displaced by 2.4 % of the lattice constant and the selenium atoms displaced parallel to the plane of the layer by 0.8 % of the lattice constant, both at 77 K. It is important to emphasize that the simulation of the electron diffraction pattern of the sample at this low temperature contain-

ing these exotic features of charge density waves has never been done before, to the best of our knowledge. Figure 6.5 (b) shows the low temperature electron diffraction pattern as obtained from simulation which is in good agreement with our experiment. Figure 6.5 (c) shows the electron diffraction pattern obtained from our experiment and Figure 6.5 (a) is the real-space unit cells of the sample at a low temperature phase. Refer to Table A.2 for the atomic positions used for this simulation.

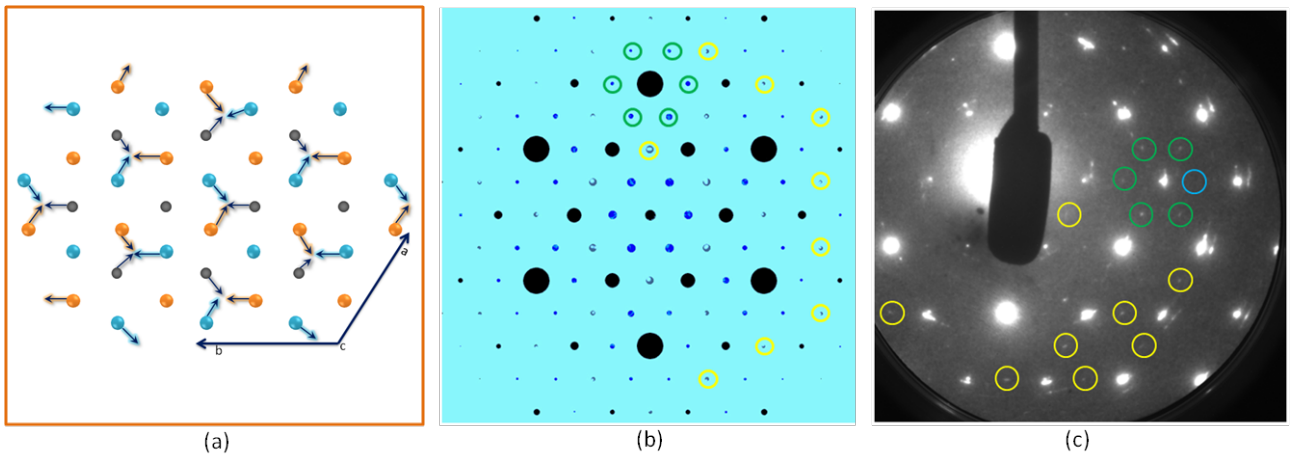

Figure 6.5: (a) A schematic representation of the real-space unit cells of the distorted phase with the blue, orange and grey colours denoting the selenium upper layer, selenium lower layer and the titanium layer respectively. Arrows indicating the displacements of atoms are not to scale. (b) Simulation showing the electron diffraction pattern at low temperature. The low temperature parameters are fed into the software and a sample thickness of 30 nm and a high voltage of 30 kV are specified. The hexagonal structure of the crystal shows a strong signature in the generated pattern revealing the commensurate superstructure or CDW spots which are depicted as grey and blue spots which are mere colour notations of the peaks. The black spots are the Bragg spots with the bigger spots indicating a constructive interference resulting from where the electron density distribution is highest in the crystal. The green and yellow circles are used to indicate CDW peaks that have been observed in the experimental pattern. (c) Electron diffraction pattern of 1*T*-$TiSe_2$ obtained from measurement at low temperature and at 30 kV for a 30 nm thick sample. The pattern also bears the signature of the hexagonal structure of the crystal. The white spots are equivalent to the black spots in (b) which are also the Bragg spots. The green and yellow circles are used to indicate CDW peaks that have been seen in the experiment as well as in the simulation with the blue circle indicating an absence of a CDW peak. The absence could be due to weaker amplitude of the peak/or sample quality. The same higher orders are revealed in both simulation and experiment contrary to Figure 6.1 (b).

Charge density wave (CDW) spots depicted as blue and grey spots are seen in between two Bragg spots and around every Bragg spot, accounting for the commensurate $2\,a_\circ \times 2\,c_\circ$ superlattice generally reported in literature with commensurate meaning that the superperiodicity developed upon phase transition is a rational multiple of the basic unit cell. Indeed, we can say that both Bragg and CDW spots bear the signatures of the hexagonal structure of the crystal. The CDW spots form a single hexagonal shape around every Bragg spot as depicted by green circles in Figure 6.5 (b) and this is also observed in the experiment with the blue circle in Figure 6.5 (c) depicting a position where a CDW peak should be seen but is absent. The absence of the CDW spot could be due to many factors: sample quality due to cutting, sample thickness and perhaps the condition during sample growth. The yellow circles depict the many CDW spots seen in between every Bragg spot in the simulation that have also been seen in the experiment.

Comparison

Unlike the room temperature phase where the orders revealed in the simulated pattern differ from that of the experiment, the orders revealed in the low temperature phase for the

simulation is the same as in the experiment. Such orders have been plotted in Figure 6.7 and are depicted as zero, first, second and third orders in Figure 6.6 (a) and (b). The reason why higher orders are now revealed at low temperature in the simulated pattern even though the sample thickness of 30 nm and an accelerated voltage of 30 kV have been used just like in the room temperature pattern is not certain. The orders however remain the same for the low temperature experimental pattern.

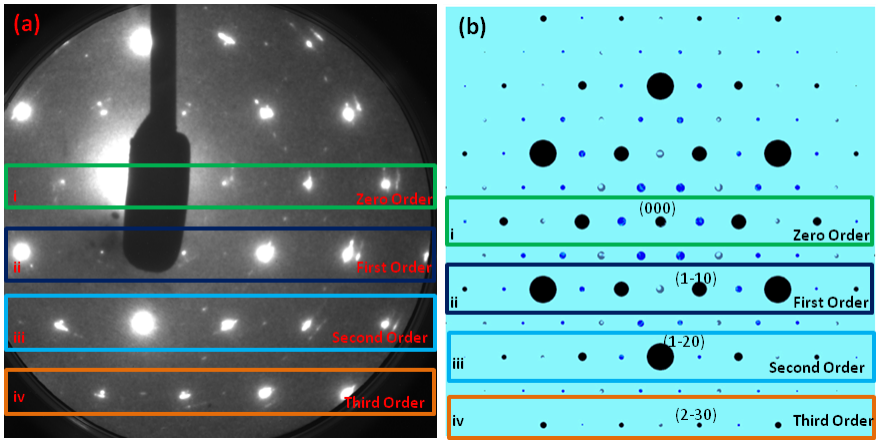

Figure 6.6: (a)i and (b)i show the zero order Bragg reflections, (a)ii and (b)ii show the first order Bragg reflections, (a)iii and (b)iii show the second order Bragg reflections and (a)iv and (b)iv show the third order Bragg reflections. These are for the experiment and the simulation at low temperature respectively.

The non-indexed peaks in Figure 6.7 for the simulation are the CDW peaks. A notable charge density wave peak for the experiment can be seen in Figure 6.7 (d) between the peak index of (1-30) and (2-30). The same argument for the appearance of peaks as explained earlier for the room temperature goes for the low temperature for Figure 6.7 (a), (b) and (c) except that there are the introduction of CDW peaks. The same number of peaks are recorded for both simulation and experiment in (d). It is important to point out that the peak index (4-30) in (d) is a new introduction in the experimental diffraction pattern compared to the room temperature experimental diffraction pattern where no such peak is seen for the same order.

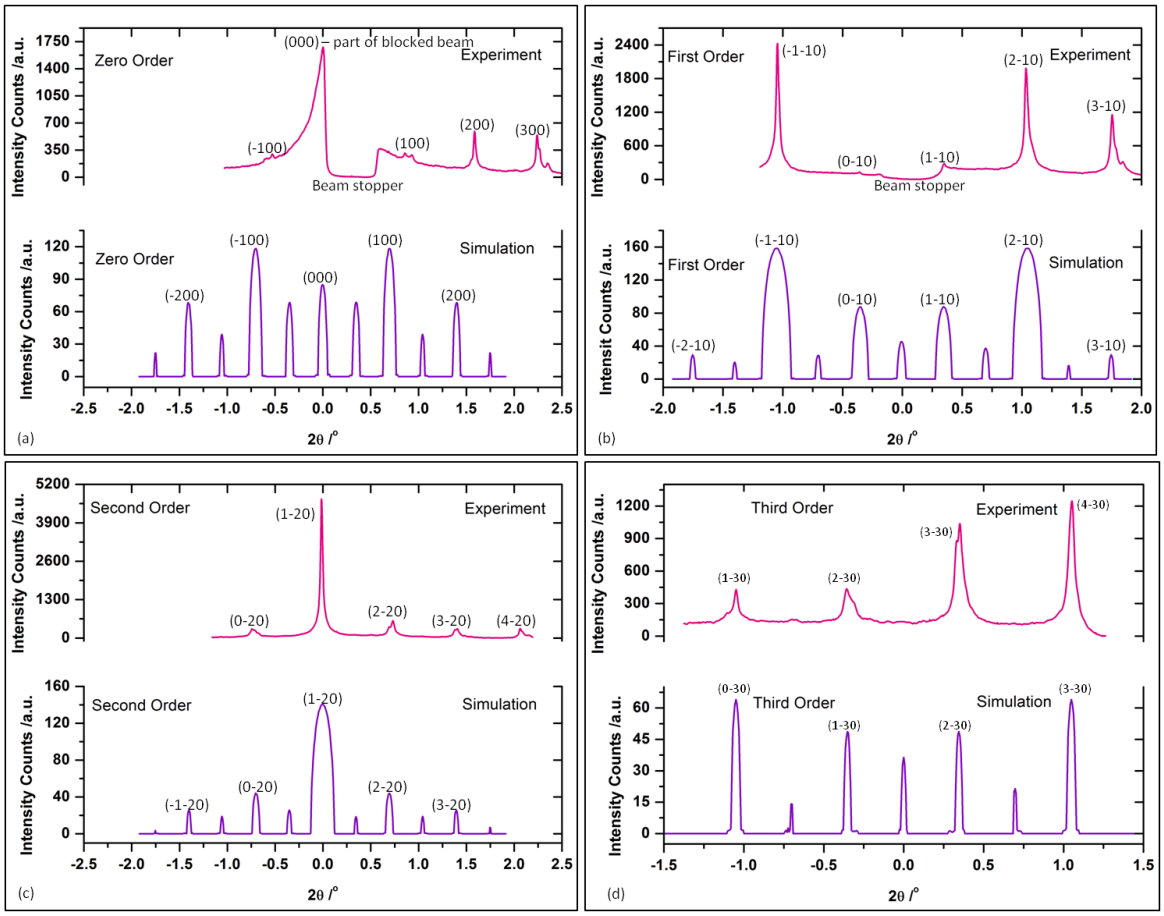

Figure 6.7: (a) A plot of Figure 6.2 (a)i and (b)i as a function 2θ showing the variation in the intensity distribution of the peaks. (b) A plot of Figure 6.2 (a)ii and (b)ii as a function 2θ showing the variation in the intensity distribution of the peaks. (c) A plot of Figure 6.2 (a)iii and (b)iii as a function 2θ showing the variation in the intensity distribution of the peaks. Note that for the experimental peaks, the CDW peaks are much harder to be seen in the graph mainly due to the extreme weakness of their amplitudes when they have to be analysed along side other Bragg spots. The peaks in the simulation that are not indexed are the CDW peaks. The graphs are for the low temperature or distorted phase.

6.4 Evolution of Superstructures with Atomic Displacements

Sometimes during cooling down of the sample to the low temperature phase, we find that the amplitude of some CDW peaks is not pronounced enough to characterise in a steady-state measurement i.e., as a function of temperature let alone perform a transient measurement. This could be due to many factors as highlighted in Section 6.3. Another factor could be due to the small displacements of atoms in the crystal. In order to have better insight into the effect of atomic displacements on the CDWs, we decreased the percentage modulation for the selenium (Se) atoms and for the titanium (Ti) atoms, from the actual atomic displacements of Ti and Se, respectively 2.4 % and 0.8 % of the lattice constant. From the original atomic displacements, it is clear that the displacement of the titanium atoms is three times that of selenium atoms. In this manner, we decreased the original percentage modulation of the selenium by a certain interval and then multiplied the results by three to get the respective percentage modulations for the titanium atoms. The results of such modulations have been simulated and these are shown in Figure 6.9.

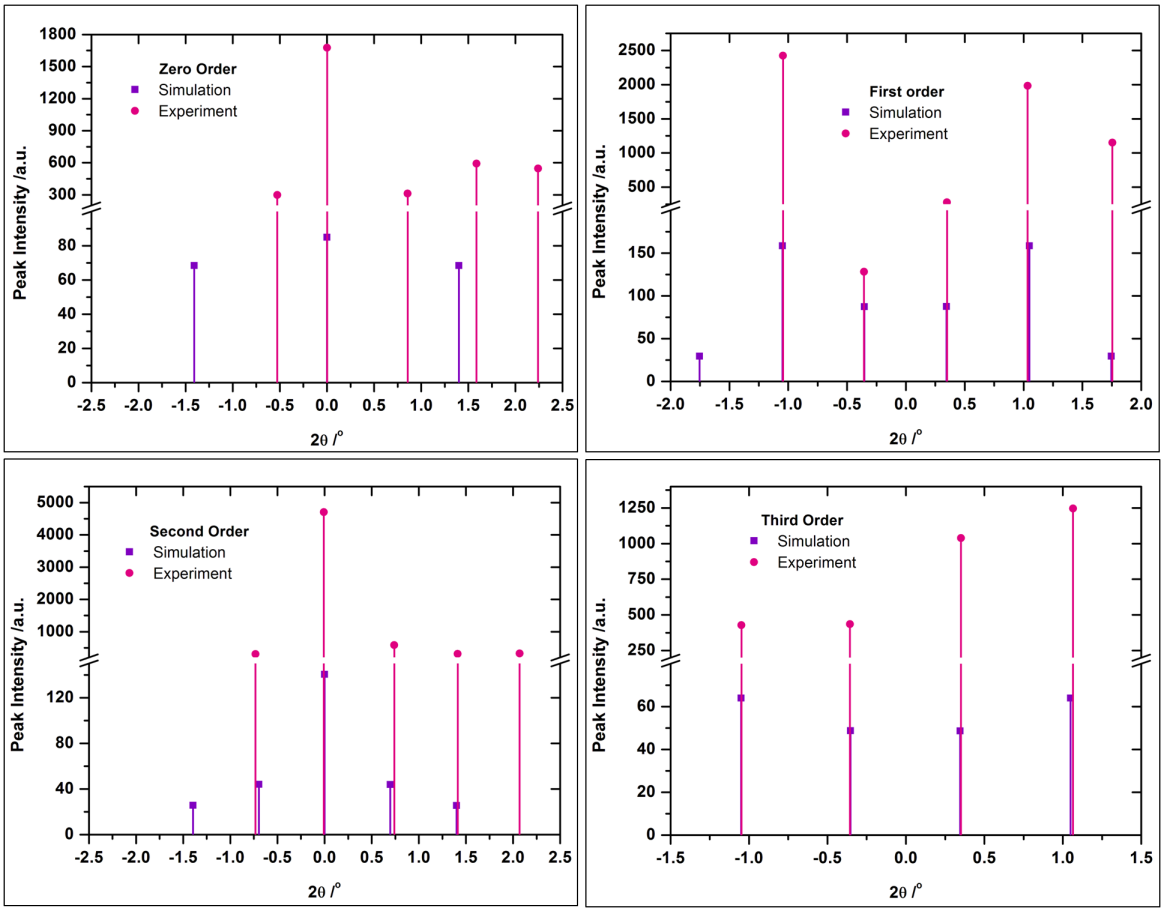

Figure 6.8: The peak intensities for Figure 6.7 have been respectively plotted as a function of 2θ showing clearly the difference in intensities between simulation and experiment. This has been plotted for all the Bragg order reflections.

A remarkable change was noticed after the first modulation which corresponds to 2.0 % and 0.67 % respectively for Ti and Se atoms as presented in Figure 6.9 (a). For example, the hexagonal superstructure surrounding the centre spot (blue) completely disappeared with reduced intensity of other superstructure spots (black spots) and some Bragg spots (red spots). This kind of superstructure disappearance around the centre spot is observed for all other modulations. These percentage modulations have been compared with the theoretical behaviour of a CDW amplitude shown in Figure 6.10 (a). The intensity of CDW peaks actually squares the amplitude of modulation which means that the larger the selenium and the titanium atoms are displaced at low temperatures the stronger the intensity of the CDW peaks. The amplitude of modulation is the squared product of the CDW wave vector and the atomic displacement. Therefore, the lesser the modulation of the atoms the lesser the CDW peak intensity. This is indeed observed in the simulation for the smallest of the percentage modulation of 0.1 % for Ti and 0.033 % for Se in Figure 6.9 (e) where weaker or no CDW peaks are seen.

This is interesting and could have been more interesting if the respective associated temperature of these modulations could be retrieved from the simulation. In the experiment however, evolution of the charge density wave peaks have been obtained as shown in Figure 6.10 (b). The lower the temperature the stronger the amplitude of the charge density

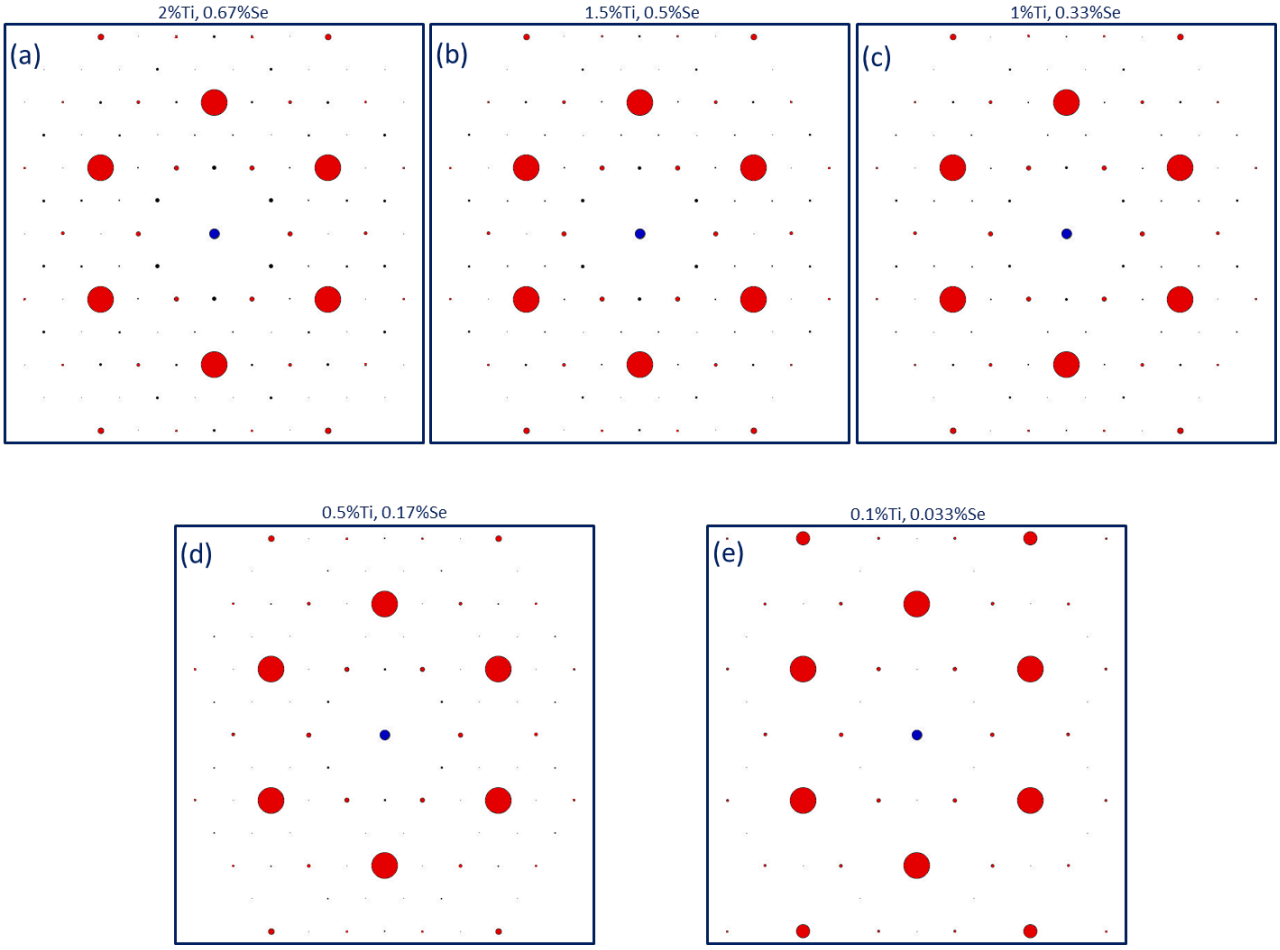

Figure 6.9: (a), (b), (c), (d) and (e) show the simulated electron diffraction pattern of the modulated titanium and selenium atoms. The percentage of modulation for both atoms are shown in their respective graphs. These percentage modulations have been derived based on the original modulation of 2.4 % Ti and 0.8 % Se atoms obtained at 77 K from [1]. It is seen that as the percentage modulation gets smaller, the superstructures get weaker or even disappear completely as it is the case for the six CDW peaks surrounding the centre spot in all of the graphs.

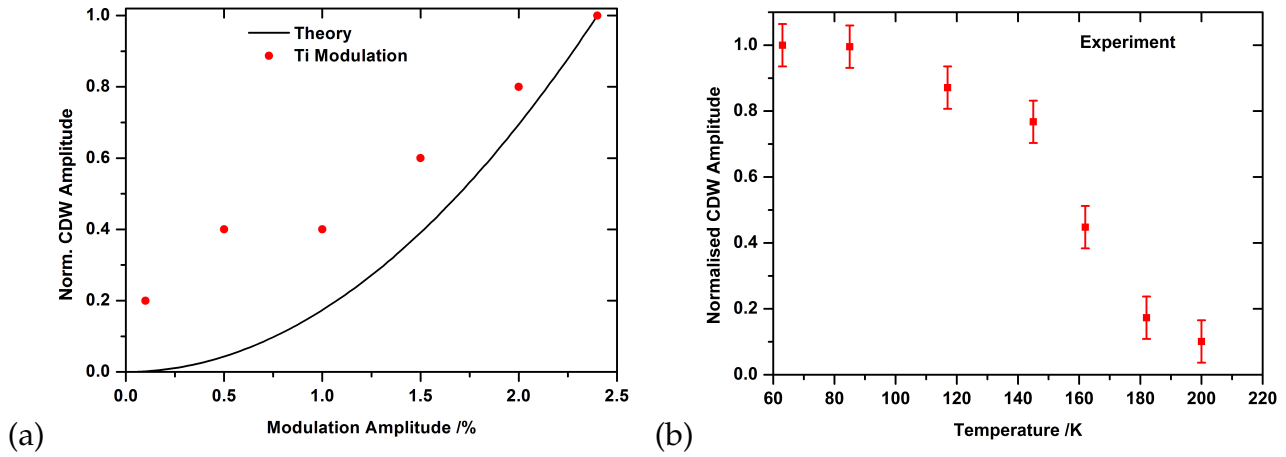

Figure 6.10: (a) The percentage modulations as simulated and presented in Figure 6.9 are being compared with the theory of modulation of CDW amplitudes for only Ti atoms. It shows that the percentage modulations do indeed follow the theoretical prediction. (b) Evolution of a charge density wave peak amplitude as a function of temperature. The amplitude increases as the temperature decreases which is an indication of an opening of a band gap at the Fermi surface. Because the appearance of charge density waves is also a result of atomic position modulation hence one can say that the increase in amplitude is the result of an increase in the atomic displacements. Note that the temperature of the sample was regulated using a cryostat at a cooling rate of 2 K/min, and the term CDW amplitude simply means the intensity of the diffraction peaks due to the CDWs.

wave peak which means that the atomic displacements get larger. The simulation result also shows that the charge density wave peak amplitude drops as the atomic displacements get smaller and vice versa.

It is nonetheless intuitive to say that even though the sample undergoes a phase transition, if the atomic displacements are not large enough one is less likely to see the signatures of the charge density wave peaks no matter how low one has to cool down. And this is indeed what the results in Figure 6.9 have portrayed.

6.5 Charge Density Wave Amplitude: Simulation and Experiment

One of the difficulties faced in performing a time-resolved measurement on our sample is the extreme weakness of its CDW amplitude. In this section, we take a look at the CDW amplitude obtained from simulation and experiment. It has been reported by Di Salvo *et al.* in [1] that the strongest CDW peak is 10^{-2} or $\sim 1\,\%$ of the normal phase strongest Bragg spot (though the exact CDW peak index for which the amplitude is determined is not specified). The strongest CDW peak we measured has an intensity of $\sim$0.28 % of the undistorted brightest Bragg spot and a peak index of (-3/2 3 0). The same peak index however shows 43 % of the brightest Bragg spot in our simulation. Another CDW peak index of (-1/2 3 0) has an intensity of $\sim$0.24 % of the brightest Bragg spot and the same peak index from simulation has an amplitude of 19 % of the undistorted brightest Bragg spot. This is shown in Figure 6.11. This kind of weakness in the CDW amplitude from our measurement has been a major limiting factor against an in-depth measurement of the structural dynamics of the crystal. Note that the amplitudes of the CDWs obtained from experiment are a result of averaging ten images meaning that it was much harder to observe any CDW peak from a single image taken. The simulation values have been obtained from the modulation of titanium atoms and selenium atoms at 77 K [1] which are 2.4 % and 0.8 % of the lattice constant of the 1T-$TiSe_2$.

In summary, we have presented in this part of the chapter results obtained from simulation and experiment. Also a qualitative analysis was done highlighting the basic observations from both simulation and experiment. In the following part of this chapter, a detailed discussion focusing mainly on the experimental findings shall be presented.

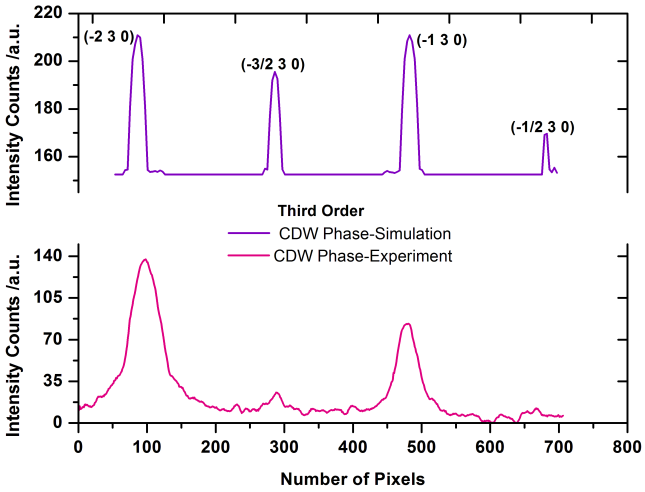

Figure 6.11: The amplitudes of CDW peaks from third order Bragg reflections for simulation and experiment at low temperature phases are being compared. The amplitude of the CDW peak for experiment was obtained at 117 K and that of simulation was at 77 K.

6.6 Experiment

In this section, we present a steady-state result regarding the room and low temperature diffraction patterns.

By analysing the intensity distributions of our experimental Bragg peaks both at room and low temperature, we find that there is little or no shift in the Bragg positions as the sample is cooled to a low temperature of 114 K. This is in agreement with what is observed in the simulation as no shift in Bragg position occurred when both phases were compared. Experimental first, second and third orders have been shown for both room and low temperature respectively in Figure 6.12. The label "CDW phase" as indicated in the figure implies the low temperature phase of 114 K. With no visible shift in Bragg position, a general drop in the peak intensities is observed for the CDW phases and most interestingly as seen in Figure 6.12 (c) for the CDW phase additional peak is introduced.

6.7 Debye-Waller Effect

We have shown in Figure 6.1 (c) and Figure 6.5 (c) the electron diffraction pattern at room temperature and at low temperature respectively from our measurements. Whilst these patterns are static ones and no information is retrievable as to how the CDWs evolve. Only a time-resolved electron diffraction measurement offers such information and this is the main focus of the thesis and its motivation. It is a technique to explore the evolution of the structural dynamics of the crystal. Meaning that we want to see how the new features called the charge density waves evolve in time and the information they carry about the crystal. Refer back to Chapter 2 for a detailed explanation.

One aspect of our time-resolved measurement focuses on the Debye-Waller factor. A term

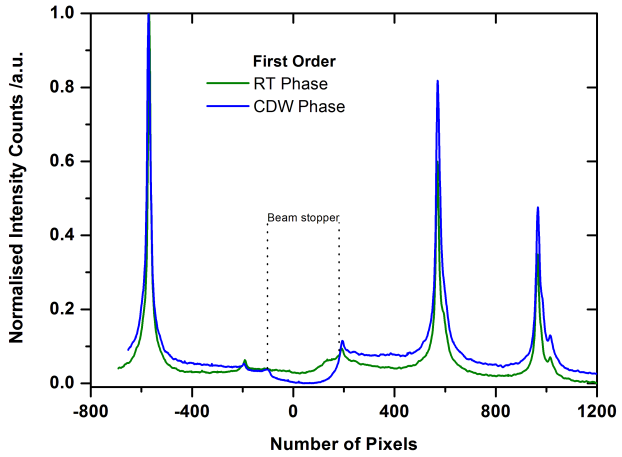

(a) Comparison between experimental electron diffraction patterns along (h10) or first order Bragg reflection for room temperature and low temperature (CDW) phases. The low temperature phase was at 114 K. It is seen that there is a slight or no shift in the position of the Bragg peaks for the low temperature phase and with the two phases containing the same number of Bragg spots except of course that there are CDW peaks in the low temperature phase whose amplitudes are too small to be seen in the graph.

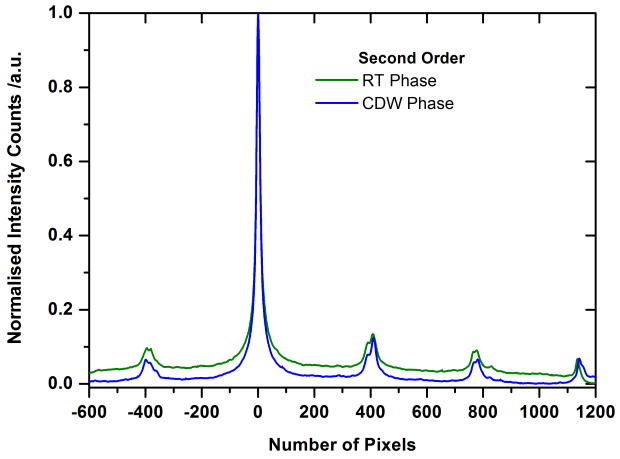

(b) Comparison between experimental electron diffraction patterns along (h20) or second order Bragg reflection for room temperature and low temperature (CDW) phases. The low temperature phase was at 114 K. The Bragg spots show little or no shift in their positions and the two phases contain the same number of Bragg spots except of course that there are CDW peaks in the low temperature phase whose amplitudes are too small to be seen in the graph.

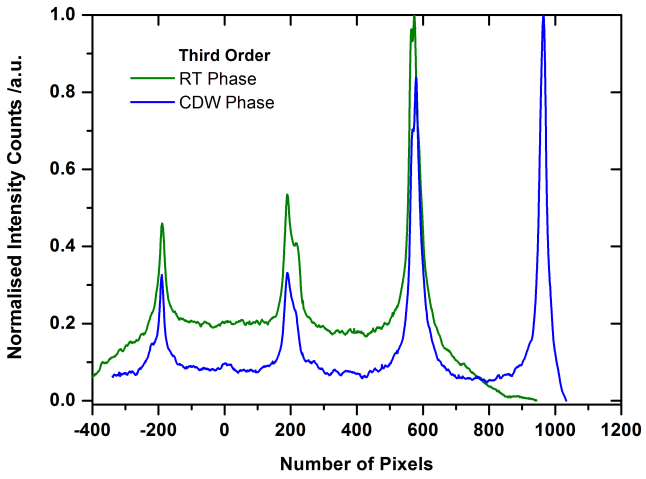

(c) Comparison between experimental electron diffraction patterns along (h30) or third order Bragg reflection for room temperature and low temperature (or CDW) phases. The low temperature phase was at 114 K. There is little or no shift in the positions of the Bragg spots but with an introduction of a new Bragg spot that is not seen in the room temperature diffraction pattern for this particular order. CDW peaks are present in the low temperature phase but cannot be seen in the graph due to their small amplitudes.

Figure 6.12: Graphs showing the intensity distribution of Bragg spots at room and low temperature. An additional peak was observed in the third order Bragg reflection for the low temperature phase. This peak was not seen in the room temperature counterpart for the same order. There is generally a drop in peak intensities for the CDW phases.

used to describe how a crystal would respond to a rising temperature. Note that our layered crystal is characterised by electron-phonon coupling. So what is a phonon and what is an electron? A phonon is a quantised lattice vibrational mode that carries energy or a quantum of vibrational energy which has resulted from atoms in a solid or crystal due to their vibrations. To simplify this definition further, let us assume lattice sites in a crystal for atoms. Atoms in these sites which are linked together and cannot vibrate independently undergo

some form of vibrations due to thermal energy present in the lattice. These collective modes or waves propagate through the crystal as mechanical waves with definite energy and momentum, hence they are called a phonon. An electron in its simplest term can be regarded as a tiny particle of matter that possesses a negative charge and revolves around the nucleus of an atom that it is present in. In a crystal, electrons are delocalised and their energy is described by a band structure.

Therefore, as energy is deposited (due to laser pumping) into the crystal, an incoherent vibration of the lattice is initiated mainly due to energy transfer from the electronic system to the lattice caused by the coupling of electrons and phonons. Thus resulting in decrease in Bragg signal/or CDW signal. The drop in both signals is due to the fact that there is a temperature increase due to laser heating which causes the atoms to vibrate about their mean position with larger amplitudes. This effect is the Debye-Waller effect and the Debye-Waller equation used for the plot in Figure 6.13 is given below:

$$I_{\mathrm{hkl}} = I_{\circ}\exp\left(-\frac{< u^2 > G^2_{\mathrm{hkl}}}{3}\right),$$

where $< u^2 >$ is the mean square displacement of an atom that is related to $k_B T$ and G is the reciprocal lattice vector. The exponential factor is the Debye-Waller factor [46] which relates to temperature. The oscillator frequency used is obtained from [47].

The actual interest in Debye-Waller effect is to be able to estimate the increase in temperature in the crystal due to energy deposition. Figure 6.13 (a) is the plot from the Debye-Waller equation utilising 1T-$TiSe_2$ parameters such as the oscillator frequency [47] showing the temperature dependence of the reflected intensities for different reflections. Figure 6.13 (b) shows the indexed pattern of the simulation. The particular peak orders that have been plotted are indicated by the circles in the said figure. Each circle has corresponding colours used in the plot. Though only one peak order indicated by the blue circle will be focused on.

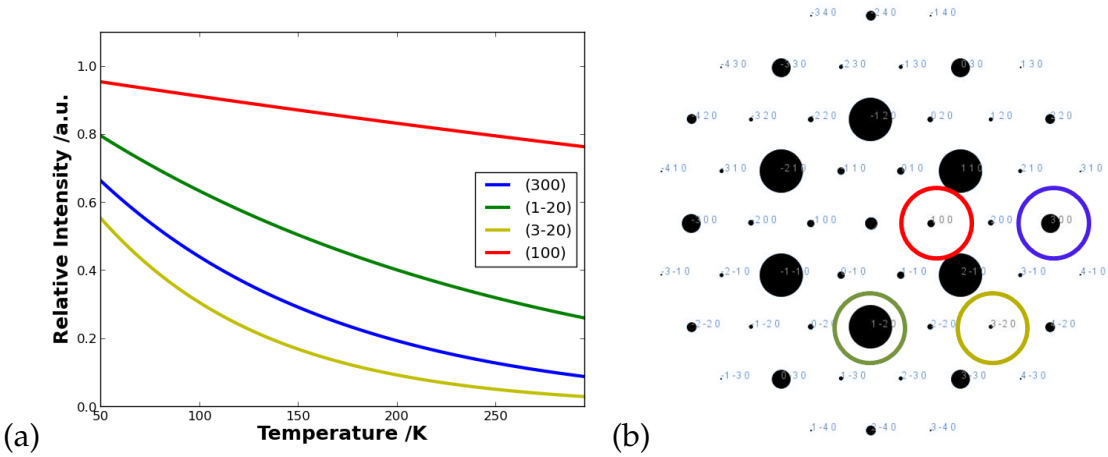

Figure 6.13: (a) A plot from Debye-Waller equation showing Debye-Waller effect for various reflection orders. It is seen that as the temperature increases the intensity drops due a shift from equilibrium by the atoms in the crystal. The higher the order the lower the scattering intensity but not necessarily seeing a dramatic change in the scattering angle. (b) Indexed electron diffraction spots obtained from simulation. The red, blue, green and lemon green circles highlight the peak orders that have been plotted in (a).

It is interesting to see that indeed there is a drop in the reflected lines as the temperature increases as seen in the Debye-Waller plot. Also, reflections of low G, where G is the reciprocal lattice vector associated with the peak orders, are less affected than the high G reflections.

6.8 Temperature Estimation from the Debye-Waller Equation

We have a sample that is at a temperature of 60 K and is photo-excited with a pump fluence of 1.3 mJ/cm^2. The electrons in the lattice receive the energy which is transferred to the atoms in the lattice. The consequence of this is that there is first a coherent vibration initiated but this is faster than we can resolve before the onset of an incoherent vibration of the lattice due to energy deposition from the laser. This means that atoms in their equilibrium position have increased their amplitude in that state as they vibrate thereby causing a drop in the Bragg signal by about 7 % as seen in Figure 6.14 (b). This sudden drop in signal occurs around time zero and a further suppression of the Bragg signal is seen. The incoherent vibration of the atoms is due to energy transfer from the electrons to the lattice resulting in a rise in temperature. To determine this temperature rise however is not trivial for highly correlated materials such as our sample. With our Debye-Waller factor approach shown for a peak order of (300) in Figure 6.14 (a) we are able to estimate a temperature rise of $\sim$64 K in our sample. A similar temperature rise has been estimated for the remaining three peak orders: (1-20), (3-20), and (100) respectively depicted as green, lemon green and red circles in Figure 6.13. Interestingly, a temperature increase in the sample due to photo-excitation at a certain fluence has been estimated in a transient x-ray measurement for a fluence of 1.2 mJ/cm^2 by [22] for a sample at 90 K and 140 K to be 56 K and 46 K respectively. This is quite in good agreement with our calculation. The standard deviation or error has been calculated to be $\pm$0.038 and since each data point is the result of averaging over five scans, the error is then $\pm$0.017.

The Debye-Waller equation used for the estimation is given below:

$$I_{\mathrm{hkl}} = I_{\circ}\exp\left(-\frac{< u^2 > G^2_{\mathrm{hkl}}}{3}\right),$$

where $< u^2 >$ is the mean square displacement of an atom that is related to $k_B T$ and G is the reciprocal lattice vector. The exponential factor is the Debye-Waller factor [46] which relates to temperature. The oscillator frequency used is obtained from [47]. Also refer to Appendix A.3.

We could also for estimate the temperature increase by using the relation below [10]:

$$\Delta T = \frac{AF}{C_v d},$$

where A is the absorption, F is the energy deposited on the crystal in terms of fluence, C_v is the volumetric heat capacity and d is the thickness of the sample. The volumetric heat capacity can be calculated from the molar heat capacity by dividing by the molar volume. The molar volume itself is the volume of the unit cell multiplied by the Avogadro's number. For $1T$-$TiSe_2$ the reflectivity at 77 K is 65 % [48]. With an optical penetration depth of 20 nm the absorption was calculated to be 13 % for a sample thickness of 30 nm. Given a volumetric heat capacity of $0.56\,J/cm^3K$ [27] and a fluence of $1.3\,mJ/cm^2$, the temperature increase ΔT was estimated to be around 100 K.

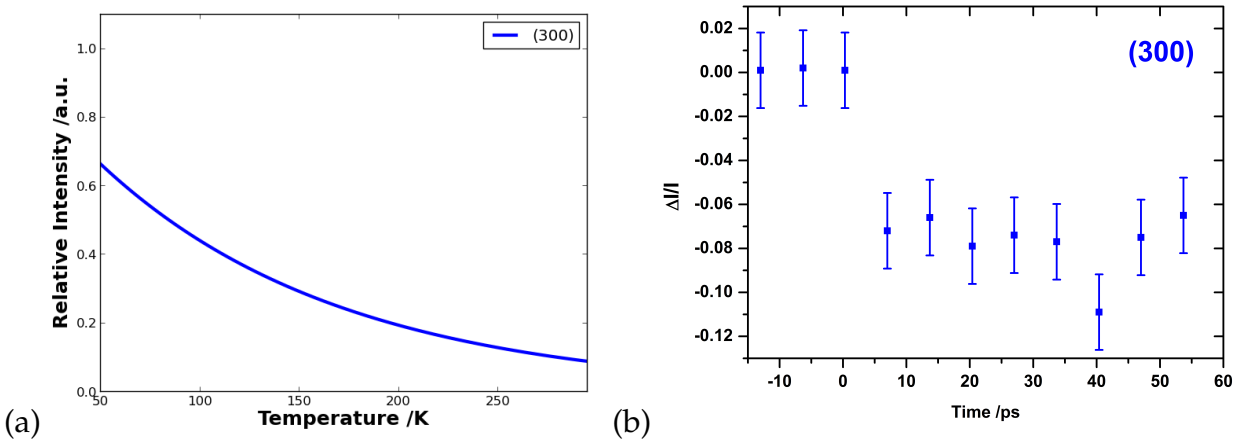

Figure 6.14: (a) Plotted Debye-Waller factor or equation for a peak order of (300). This is to be compared with the same experimental peak order in order to extract the temperature increase in the crystal. (b) Experimental Debye-Waller effect for the peak order in (a) with the sample at 60 K and has been photo-excited with a pump fluence of $1.3\,mJ/cm^2$. A temperature increase of 64 K was obtained.

Still on the Debye-Waller effect, a separate sample (still the $1T$-$TiSe_2$) cooled to 94 K was illuminated at a pump fluence of around $2.5\,mJ/cm^2$ and also shows the incoherent vibration process taking place in the crystal. See Figure 6.15. The same trend of decrease in Bragg signal is observed as in Figure 6.14 (b). The Bragg signal decreases by around 10 % of its original signal with further decay at a longer timescale. Temperature increase in this particular sample at the said temperature and fluence has not been determined using Debye-Waller equation and this is due to the fact that for this particular result, six different orders of Bragg peaks have been analysed together. The fitting to the data points have been done based on the two functions shown below and a time constant of ~2 ps for the incoherent process was obtained. It is important to emphasize that this time constant is associated with materials with strong electron-phonon coupling. The error bar in this case has been calculated to be ± 0.024 with a standard deviation of ± 0.058. Each data point is the result of averaging over six scans.

The following functions were used in the fit to the measured data in Figure 6.15.

Step Function

The step function as used here is to set the data points before time zero to zero.

$0.5 \times (\tanh(1000 \times t) + 0.5)$ and t is the time which can be expressed as $t + t_{\text{shift}}$ where t_{shift} represents the shift from time zero. This function is used to ensure that all values before time zero are set to zero.

Incoherent Processes

$\Delta I(t)/I = -a + a \times \exp(-b \times t)$, (for incoherent processes) and t is the time which can be expressed as $t + t_{\text{shift}}$ with $a = 0.13$ and $b = 0.56$ being the values generated from the fit.

The multiplication of the step function and the function for the incoherent processes gave the fitting to the data points in Figure 6.15.

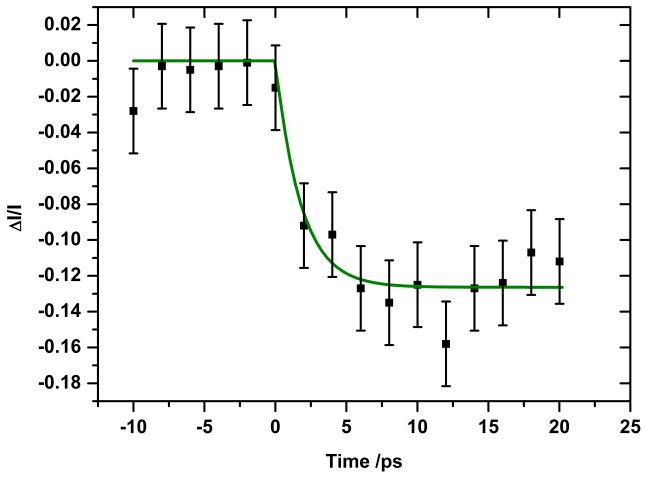

Figure 6.15: A signature of Debye-Waller effect is observed once again for a sample at 94 K and photo-excited with a pump fluence of 2.5 mJ/cm^2. There are six peak orders that have been averaged for this particular result. This means that a temperature increase at this temperature and fluence cannot be determined since our Debye-Waller equation uses information of an individual peak order.

6.9 Temperature Characterisation of a CDW Peak

Let us emphasize here that the charge density waves or superstructures are the features we are very much interested in mainly due to the fact that we can study their evolution and gain more insight into the crystal structure. Another interesting measurement we can do on the CDWs is the characterisation of its amplitude or intensity as a function of temperature. This is interesting and of importance because the appearance of CDWs due to lattice modulation is directly related to the opening of an energy gap in the crystal under investigation. Hence, the need to present this finding which is in agreement with Di Salvo *et al.* in [1]. There is also a close similarity between our measured CDW amplitude and the prediction made by the well recognised theory for describing the energy gap in a superconductor - the BCS (Bardeen-Cooper-Schrieffer) theory (Figure 6.16). It is seen in Figure 6.16 that the amplitude

of the CDW behaves in a similar manner as the theory. This kind of behaviour has also been observed for the $4H_b$TaSe$_2$ [9] - another material characterised by CDWs belonging to the same family as the $1T$-TiSe$_2$. This result is important especially due to the recent superconducting behaviour of the $1T$-TiSe$_2$ under pressure [11] and its Cu intercalation complexes [12] when cooled down to around 4 K. The CDW amplitude as it is used means the CDW peak intensity and the order parameter for the BCS theory is the normalised energy gap. Since the increase in the CDW peak intensity is due to the increase in the lattice modulation, and the CDW formation itself is as a result of energy gap opening at the Fermi surface, perhaps because of this similarity in behaviour one could possibly use the BCS theory for energy gap formation in a superconductor for the description of the CDW formation in this crystal. This observation is however with a caution as one cannot underestimate the complicated physics that is at play in the exotic phase of the crystal.

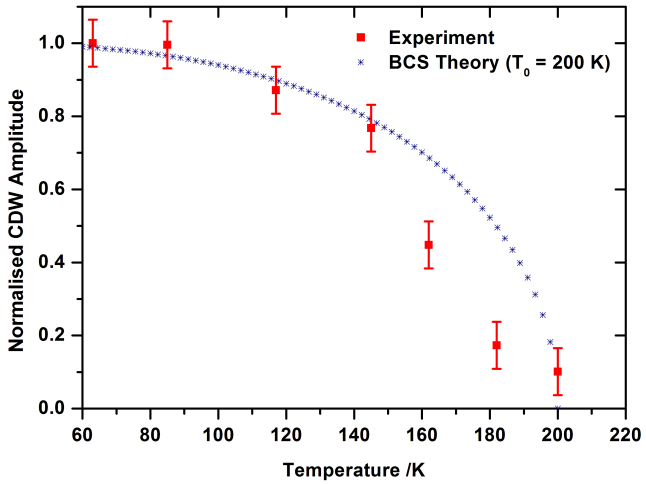

Figure 6.16: The CDW peak amplitude or intensity increases as the temperature drops below the phase transition temperature of ~200 K. A BCS theory calculation for the energy gap description in semiconductors has been compared with the measurement and shows good agreement.

It is also important to point out that ARPES study by Monney *et al.* [13] within the frame work of exciton condensate phase model shows a BCS-like behaviour of the order parameter as a function of temperature obtained from calculation and experiment. Assuming an excitonic phase transition, they set the order parameter of the crystal to 100 meV in their calculation in order to model its temperature dependence and to know what to expect in their photoemission measurements. They found from their ARPES measurements that the order parameter increases as the temperature decreases showing similar behaviour to their calculation. This finding has been attributed to the existence of exciton condensate phase in the $1T$-TiSe$_2$. The exciton condensate phase simply means that part of the conduction bands stay at the Fermi energy of the crystal when a band gap opens which leaves unperturbed states close to the Fermi energy thereby reducing its insulating character. This makes the exciton condensate phase different from the excitonic insulator phase and it is a coherent bound state of electrons and holes below the phase transition. In conventional superconductivity, there is an interaction of electrons leading to creation of Cooper pairs with some complicated physics of course whilst for an excitonic insulator phase there is already an attraction between the electrons and the holes leading to bound excitons.

In summary, the BCS theory is seen to be a vital ingredient for the understanding of CDW formation in this material.

6.10 Transient Measurement on the CDW of the 1T-TiSe$_2$

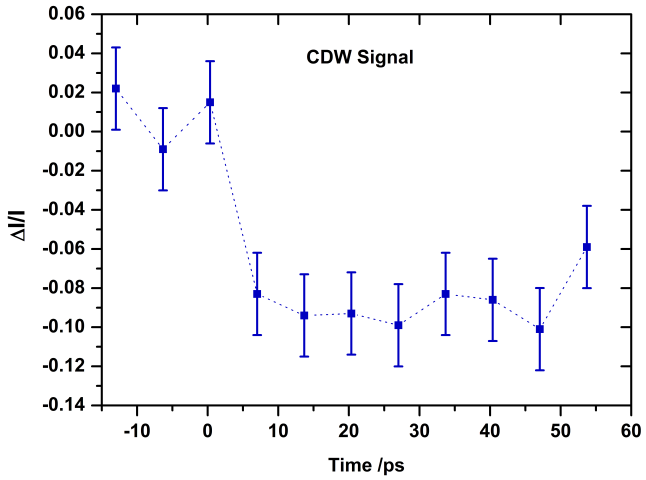

Figure 6.17: A CDW transient signal as obtained from femtosecond electron diffraction using a pump-probe method. The error bar has been calculated for the CDW signal to be ± 0.021 with a standard deviation of ± 0.047. Since each data point is the result of averaging over five scans, hence the error bar obtained.

Time-resolved measurement is the main motivation of this project due to the stated reasons earlier on in Chapter 1 and 3 and as emphasized in Section 6.9. However, there were challenges associated with performing transient measurements on the sample. One of these challenges is the sample thickness as discussed in Chapter 4. The very thin sample that we have to deal with contributes to the complication as it is difficult to get samples between 20 to 30 nm thick or less. It is necessary to keep the sample thickness as thin as possible because we want the electron beam to pass through with the 30 keV electron energy. In other words, the sample has to be electron transparent. Also, the thicker the sample the harder it becomes to observe the CDW peaks due to the weaker amplitude of the peaks, that is, if the electron beam is able to pass through the sample and this could be achieved by increasing the electron number per pulse. Hence, one is forced to cool down as low as possible since the CDW amplitude increases with decreasing temperature.

Nevertheless, we have reduced the stated challenges to an extent and have acquired a transient signal for the CDW peaks as shown in Figure 6.17. The sample was at 60 K and a fluence of 1.3 mJ/cm^2 was used for the photo-excitation. We see an incoherent decay of the CDW signal which is onset around 0 ps-7 ps with a continuous decay. The initial drop in the CDW signal is around 10.5 %. Because it was challenging to acquire data in order to have more data points so that an appropriate data fit could be carried out, from which information regarding the evolution of the CDW peak can be obtained, further measurements are necessary. Such measurements are expected to help answer some of the lingering questions surrounding the formation of CDWs in this material. The error bar has been calculated for the CDW signal to be ± 0.021 with a standard deviation of ± 0.047. Note that each data point in the figure is a result of averaging over five images.

In summary, the Debye-Waller measurement shows evidence for electron-phonon coupling due to the time constant of 2 ps obtained for the 1T-$TiSe_2$ that is typical of materials that show strong electron-phonon coupling. This evidence points to Peierls instability as a possible mechanism driving the CDW formation. To strongly establish this, further measurements are necessary. Temperature increase in the crystal due to photo-excitation was also obtained. No precise conclusion can be drawn from the transient signal of the CDW peak as more data points are needed to do the necessary fit so that more information can obtained. Characterising the CDW peak for different fluences could reveal more information regarding the mechanism behind the CDW formation in the crystal.

It is important to emphasize that the results presented in this work cannot categorically answer some of the lingering issues surrounding the driving force behind the formation of the CDWs in this material as introduced in Chapter 1, but, to rather add to the pool of knowledge already available on this crystal.

We have presented concisely in this chapter the results obtained from a steady-state electron diffraction patterns for simulation and experiment and have performed time-resolved measurement on the polytype 1T-$TiSe_2$ as an initial result using time-resolved femtosecond electron diffraction technique.

7. Summary

The motivation for this project was to use an experimental tool based on femtosecond electron diffraction to study the structural dynamics of strongly correlated 1T-$TiSe_2$. To observe the structural dynamics of the crystal, it requires that a short laser pulse known as the pump pulse excites the crystal and an electron pulse known as the probe pulse takes a snap shot of a structural evolution. Because there is a delay between the pump pulse and the probe pulse, such evolution of the structures can be observed in time. We have used this experimental method to successfully study the crystal. In addition, simulations have also been used to obtain the room temperature and low temperature electron diffraction patterns of the sample.

The first part of the investigation was focused on the simulation of the sample generating the electron diffraction pattern with a software programme called Simulation and Analysis of Electron Diffraction (SAED). The simulated diffraction patterns for both room and low temperature gave a good insight as to what should be expected in the steady-state experimental results. Nicely distributed charge density wave (CDW) spots in between the Bragg spots and around the Bragg spots have been seen for the low temperature simulations.

The second part of the investigation was focused on the experimental study. Electron diffraction patterns using a femtosecond electron diffraction technique were obtained and low temperature features such as the CDWs have been observed. Steady-state measurements such as the temperature characterisation of the intensity of the Bragg spots as well as the CDW spots were carried out. The effect of Debye-Waller due to photo-excitation of the sample and a temperature rise as a result of such illumination were observed and obtained respectively. The first ever reported transient signal of 1T-$TiSe_2$ to be observed using femtosecond electron diffraction based on a pump-probe technique was carried out. Comprehensive analysis of both the simulated and experimental patterns have been performed and the results shown. This presents a first step towards the final goal of answering the questions around the CDW origins by using femtosecond electron diffraction.

Extensive insight into the sample preparation was presented. Because a very thin sample needs be achieved for our technique, an ultramicrotome stationed at Stellenbosch University Central Analytical Facilities (CAF) has been used for this purpose and the thin samples were specially collected by floating the film onto a square grid TEM mesh.

Outlook

With a new ultra high vacuum chamber currently in place in our ultrafast laboratory and now fully functional, it is hoped that further in-depth study of this crystal will be carried out under new improved experimental conditions such as a very low pressure thereby reducing condensation problems encountered in the current setup as well as minimising the time required to carry out an experimental task. Also, with the implementation of an electron pulse compressor currently being developed, better temporal resolution could be achieved. This means that single shot experiments could be possible, reducing the experimental time significantly.

A. Other Useful Information

A.1 2.4 % Ti and 0.8 % Se Atom Displacements

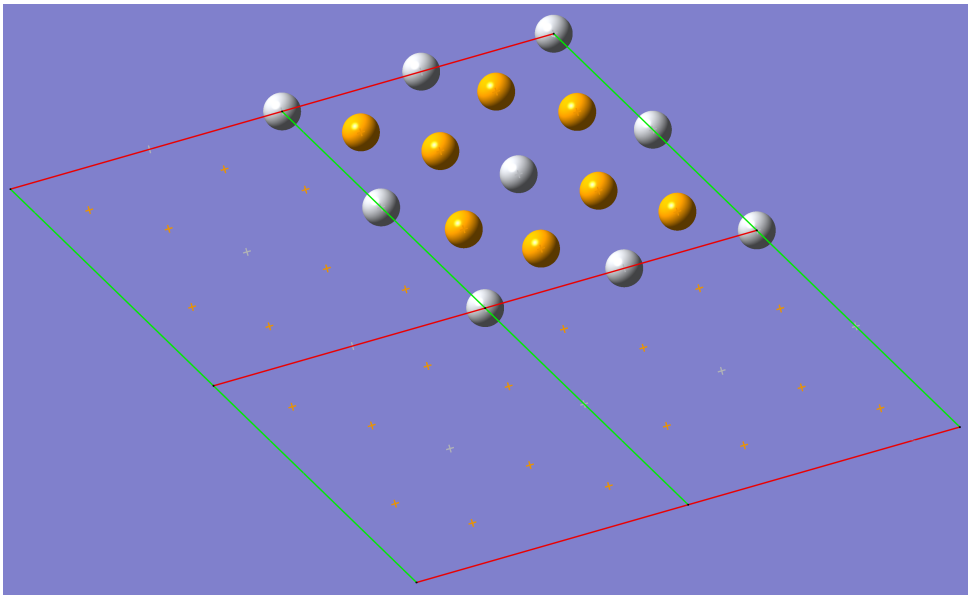

Figure A.1: Modulated unit cell of 1*T*-$TiSe_2$. The modulation has been done according to the displacements of Ti and Se atoms reported in [1]. This is a 2a $\times$ 2b $\times$ 2c modulated unit cells. The region with solid balls is the region fed to the simulation programme. Other regions are just for visual purposes. The grey solid balls denote the titanium (Ti) atoms and the yellow solid balls denote the selenium (Se) atoms.

Table A.2 shows the generated atomic coordinates according to Figure A.1. Note that the modulation is done based on the room temperature atomic coordinates in Table A.1. In other words, the atomic coordinates in the table have been calculated based on how the various titanium and selenium atoms have moved as reported by Di Salvo *et al.* but using the room temperature atomic coordinates.

	x	y	z
Ti atom	0.0	0.0	0.0
Se atom	1/3	2/3	0.25504

Table A.1: Room temperature atomic coordinates as obtained from [6].

	x	y	z
Ti atom	0	0	0
″	0.4880	0	0
″	1	0	0
″	0	0.4880	0
″	0.5120	0.5120	0
″	1	0.4880	0
″	0	1	0
″	0.4880	1	0
″	1	1	0
Se atom	0.1627	0.3334	0.1275
″	0.3334	0.1707	0.3725
″	0.8374	0.1707	0.3725
″	0.6667	0.3334	0.1275
″	0.3334	0.6667	0.3725
″	0.1707	0.8374	0.1275
″	0.6667	0.8294	0.1275
″	0.8294	0.6667	0.3275

Table A.2: Generated atomic coordinates for the low temperature unit cell. These atomic coordinates have been used in the simulation to generate the low temperature electron diffraction pattern where CDW peaks were clearly seen and are in agreement with Brillouin zones shown for the commensurate 1T-$TiSe_2$ in [15].

A.2 Beam Parameters

Gaussian beam width or spot size variation as a Gaussian beam propagates in free space is given by

$$w(z) = w_0\sqrt{1+\left(\frac{X}{X_R}\right)^2}.$$

Rayleigh range can also be defined as

$$X_R = \frac{\pi w_0^2}{\lambda}.$$

The beam radius at one Rayleigh distance from the beam waist can also be defined as

$$w(\pm X_R) = \sqrt{2}w_0.$$

Depth of focus, otherwise known as confocal parameter, can be determined as:

$$b = 2X_R.$$

Beam divergence defined as the angle between the straight line at w(z) and z = 0 which is at the beam waist (refer to Figure 5.10) is given by

$$\theta = \frac{\lambda}{\pi w_0},$$

with θ in radians.

The total angular spread of the beam far from the waist is now

$$\Theta = 2\theta.$$

Because the origin can be approximated by a point source, therefore

$$\Theta = \frac{D}{F},$$

with D the diameter illuminated on the lens and F the focal length.

A.3 Debye Waller Equation:

$$I_{\text{hkl}} = I_{\circ}\exp\left(-\frac{< u^2 > G_{\text{hkl}}^2}{3}\right),$$

where $< u^2 >$ is the mean square displacement of an atom given by $\frac{3K_BT}{M\omega^2}$ and G is the reciprocal lattice vector. Thus,

$$I_{\text{hkl}} = I_{\circ}\exp\left(-\frac{k_BTG_{\text{hkl}}^2}{M\omega^2}\right),$$

with I the scattered intensity, M the mass of $1T$-$TiSe_2$, T the temperature and ω the oscillator frequency of 1-T-$TiSe_2$. The oscillator frequency used is obtained from [47].

A.4 Fit Function for Debye Waller Signal

Step Function

$0.5 * (\tanh(1000 * t) + 1)$ and t can be expressed as $t + t_{\text{shift}}$ where t_{shift} represents the shift from time zero. This function is used to ensure that all values before time zero are set to zero.

Incoherent Processes

$\Delta I(t)/I = C(1 - exp(-t/\tau_{\text{icoh}})$, with $C < 0$ (for incoherent processes) and t can be expressed as $t + t_{\text{shift}}$.

The fit function is therefore the multiplication of the two defined functions. This function convoluted with temporal response of experiment, can be used to fit the transient signal of the Bragg peak as well as the CDW peak. In this case, the sum of coherent and incoherent exponential functions are used for both cases. See [9].

A.5 The Streak Camera and the Vacuum Chamber

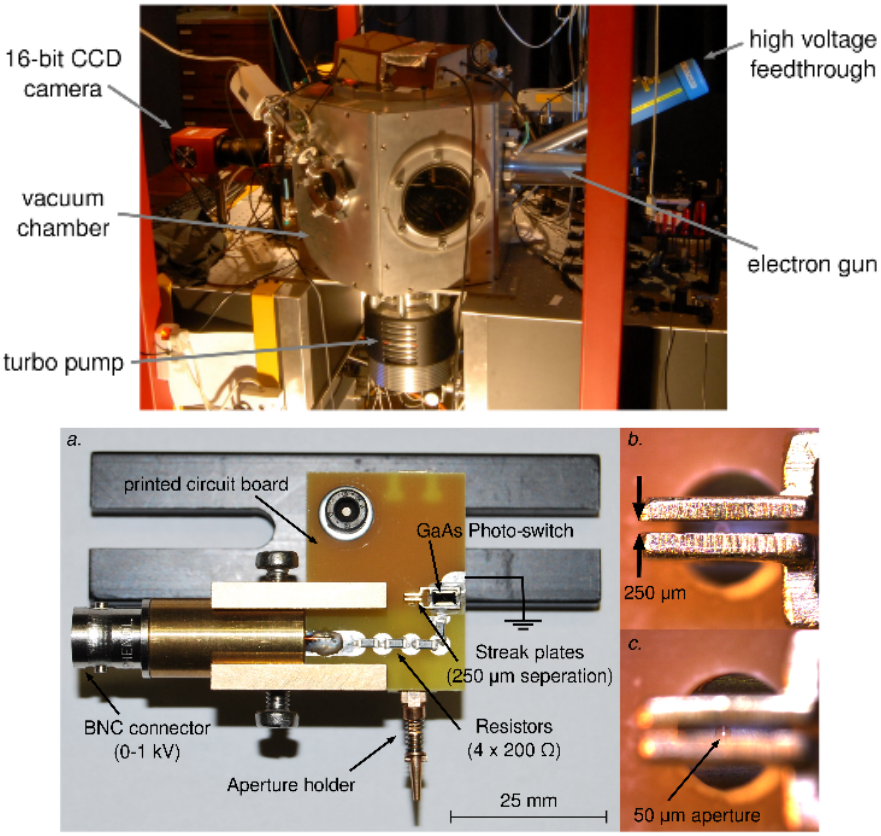

Figure A.2: Upper: The vacuum chamber showing other components necessary to carry out a femtosecond electron diffraction measurement. The MCP and the phosphor screen are integrated together and resides inside the chamber. The window outside the chamber leading to the MCP/phosphor or the detector is where the 16-bit CCD camera is positioned. Lower: The streak camera used for measuring the pulse duration. The streaking plates are 250 µm apart and an aperture of 50 µm attached to the streaking plates for easy electron beam optimisation [9].

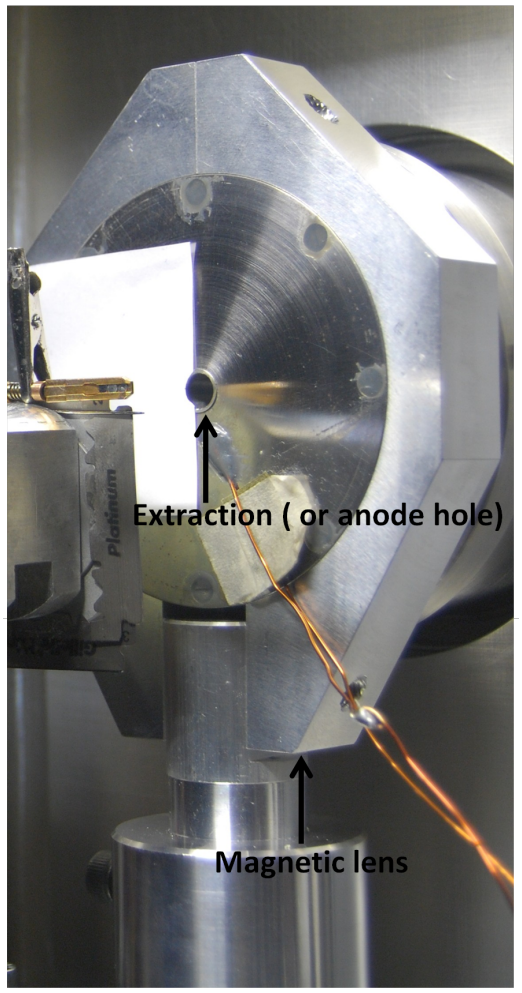

Figure A.3: The magnetic solenoid lens in the vacuum chamber showing the extraction opening for the electron beam. The extraction opening is linked to the anode hole. The magnetic lens sits on a stand which is in turn screwed to the chamber base.

Bibliography

[1] Salvo, F.J.D., Moncton, D.E. and Waszezak, J.V.: Electronic properties and superlattice formation in the semimetal $TiSe_2$. *Physical Review B*, vol. 14, no. 10, pp. 4321–4328, 1976.

[2] Rasch, J.C.E., Stemmler, T., Müller, B., Dudy, L. and Manzke, R.: $1T$-$TiSe_2$: Semimetal or semiconductor? *Physical Review Letters*, vol. 101, no. 23, pp. 1–4, 2008.

[3] Li, G., Hu, W.Z., Qian, D., Hsieh, D., Hasan, M.Z., Morosan, E., Cava, R.J. and Wang, N.L.: Semimetal to semimetal charge density wave transition in $1T$-$TiSe_2$. *Physical Review Letters*, vol. 99, p. 027404, 2007.

[4] Hellmann, S., Rohwer, T., Kallne, M., Hanff, K., Sohrt, C., Stange, A., Carr, A., Murnane, M., Kapteyn, H., Kipp, L., Bauer, M. and Rossnagel, K.: Time-domain classification of charge-density-wave insulators. *Nature Communications*, vol. 3, p. 1069, 2012.

[5] Li, X.: Simulation and analysis of electron diffraction. SAED `http://www.unl.edu/ncmn-cfem/xzli/programs.htm`, Accessed in August 2014.

[6] Riekel, C.: Structure refinement of $TiSe_2$ by neutron diffraction. *Journal of Solid State Chemistry*, vol. 17, pp. 389–392, 1976.

[7] Gronvold, F. and Langmyhr, F.J.: X-ray study of titanium selenides. *Acta Chemica Scandinavica*, vol. 15, no. 10, pp. 1949–1962, 1961.

[8] Erasmus, N., Eichberger, M., Haupt, K., Boshoff, I., Kassier, G., Birmurske, R., Berger, H., Demsar, J. and Schwoerer, H.: Ultrafast dynamics of charge density waves in $4H_b$-$TaSe_2$ probed by femtosecond electron diffraction. *Physical Review Letters*, vol. 109, p. 167402, 2012.

[9] Erasmus, N.: *Ultrafast Structural Dynamics in $4H_b$-$TaSe_2$ Observed by Femtosecond Electron Diffraction*. PhD, Stellenbosch University, 2013.

[10] Haupt, K.: *Phase Transitions in Transition Metal Dichalcogenides Studied by Femtosecond Electron Diffraction*. PhD, Stellenbosch University, 2013.

[11] Kusmartseva, A.F., Sipos, B., Berger, H., Forro, L. and Tutis, E.: Pressure induced superconductivity in pristine $1T$-$TiSe_2$. *Physical Review Letters*, vol. 103, p. 236401, 2009.

[12] Morosan, E., Zandbergen, H.W., Dennis, B.S., Bos, J.W.G., Onose, Y., Klimczuk, T., Ramirez, A.P., Ong, N.P. and Cava, R.J.: Superconductivity in Cu_xTiSe_2. *Unpublished*.

[13] Monney, C., Schwier, E.F., Garnier, M.G., Mariotti, N., Didiot, C., Beck, H., Aebi, P., Cercellier, H., Marcus, J., Battaglia, C., Berger, H. and Titov, A.N.: Temperature-dependent photoemission on $1T$-$TiSe_2$: Interpretation within the exciton condensate phase model. *Physical Review B*, vol. 81, p. 155104, 2010.

[14] Morales, J.: *Charge density waves: An emergent ground state in the manganites*. Paper, Department of Physics and Materials Research Laboratory, University of Illinois at Urbana-Champaign, Urbana, Illinois 61801, 2009.

[15] Rossnagel, K.: On the origin of charge-density waves in select layered transition-metal dichalcogenides. *Journal of Physics: Condensed Matter*, vol. 23, no. 21, pp. 1–24, 2011.

[16] Jaswal, S.S.: Lattice dynamics of $TiSe_2$. *Physical Review B*, vol. 20, no. 12, pp. 5297–5300, 1979.

[17] Vorobeva, E., Johnson, S.L., Beaud, P., Staub, U., Souza, R.A.D., Milne, C.J., Ingold, G. and Titov, A.N.: Laser induced melting in $TiSe_2$: Optical and x-ray study. *OSA*, 2010.

[18] Woo, K.C., Brown, F.C., McMillan, W.L., Miller, R.J., Schaffman, M.J. and Sears, M.P.: Superlattice formation in titanium diselenide. *Physical Review B*, vol. 14, no. 8, pp. 3243–3247, 1976.

[19] Goli, P., Khan, J., Wickramaratne, D., Lake, R.K. and Balandin, A.A.: Charge density waves in exfoliated films of van der waals materials: Evolution of Raman spectrum in $TiSe_2$. *Nano Letters*, vol. 12, pp. 5941–5945, 2002.

[20] Holt, M., Zschak, P., Hong, H., Chou, M.Y. and Chiang, T.C.: X-ray studies of phonon softening in $TiSe_2$. *Physical Review Letters*, vol. 86, no. 17, pp. 3799–3802, 2001.

[21] Holt, M.V.: *X-Ray Studies of Lattice Dynamics*. PhD, Graduate College of the University of Illinois at Urbana-Champaign, Urbana, Illinois, 2002.

[22] Möhr-Vorobeva, E., Johnson, S.L., Beaud, P., Staub, U., Souza, R.D., Milne, C., Ingold, G. and Demsar, J.: Nonthermal melting of a charge density wave in $TiSe_2$. *Physical Review Letters*, vol. 107, no. 3, pp. 1–4, 2011.

[23] Cercellier, H., Monney, C., Clerc, F., Battaglia, L., Garnier, M.G., Beck, H., Aebi, P., Patthey, L., Berger, H. and Forró, L.: Evidence for an excitonic insulator phase in $1T$-$TiSe_2$. *Physical Review Letters*, vol. 99, no. 14, pp. 1–4, 2007.

[24] May, M.M., Brabetz, C., Janowitz, C. and Manzke, R.: Charge-density-wave phase of $1T$-$TiSe_2$: The influence of conduction band population. *Physical Review Letters*, vol. 107, pp. 176405–1 – 176405–4, 2011.

[25] May, M.M., Brabetz, C., Janowitz, C. and Manzke, R.: Angle-resolved photoemission studies of the band structure of $TiSe_2$ and TiS_2. *Physical Review B*, vol. 21, no. 2, pp. 615–624, 1980.

[26] Greenaway, D.L. and Nitsche, R.: Preparation and optical properties of group IV-VI_2 chalcogenides having the CdI_2 structure. *J. Phys. Chem. Solids*, vol. 26, pp. 1445–1458, 1965.

[27] Craven, R.A., Salvo, F.J.D. and Hsu, F.S.L.: Mechanisms for the 200 K transition in $TiSe_2$: A measurement of the specific heat. *Solid State Communications*, vol. 25, pp. 39–42, 1978.

[28] Baranov, N.V., Inoue, K., Maksimov, V.I., Ovchinnikov, A.S., Pleschov, V.G., Podlesnyak, A., Titov, A.N. and Toporova, N.V.: Ni intercalation of titanium diselenide: effect on the lattice, specific heat and magnetic properties. *Journal of Physics: Condensed Matter*, vol. 16, p. 92439258, 2004.

[29] Ayache, C. and nez Regueiro, M.N.: Basal thermal conductivity of $TiSe_2$. *Journal De Physique*, vol. 42, no. 12, pp. c6–338–c6–340, 1981.

[30] Wilson, J.A.: Concerning the semimetallic characters of TiS_2 and $TiSe_2$. *Solid State Communications*, vol. 22, pp. 551–553, 1977.

[31] Brown, F.C.: Electronic and vibronic structure of TiS_2 and $TiSe_2$. *Physica*, vol. 99B, pp. 264–270, 1980.

[32] Rossnagel, K., Kipp, L. and Skibowski, M.: Charge density wave transition in $TiSe_2$: Excitonic insulator versus band-type Jahn-Teller mechanism. *Physical Review B*, vol. 65, no. 23, pp. 1–7, 2002.

[33] Monney, C., Schwier, E.F., Garnier, M.G., Mariotti, N., Didiot, C., Cercellier, H., Marcus, J.,

Berger, H., Titov, A.N., Beck, H. and Aebi, P.: Probing the exciton condensate phase in 1T-$TiSe_2$ with photoemission. *New Journal of Physics*, vol. 12, p. 125019, 2010.

[34] Monney, C., Battaglia, C., Cercellier, H., Aebi, P. and Beck, H.: Exciton condensation driving the periodic lattice distortion of 1T-$TiSe_2$. *Physical Review Letters*, vol. 106, p. 106404, 2011.

[35] Monney, C., Battaglia, C., Cercellier, H., Aebi, P. and Beck, H.: Temperature dependence of the excitonic insulator phase model in 1T-$TiSe_2$. *Physica B: Condensed Matter*, vol. 404, no. 19, pp. 3172–3175, 2009.

[36] Motizuki, K., Suzuki, N., Yoshida, Y. and Takaoka, Y.: Role of electron-lattice interaction in lattice dynamics and lattice instability of 1T-$TiSe_2$. *Solid State Communications*, vol. 40, pp. 995–998, 1981.

[37] Calandra, M. and Mauri, F.: Charge density wave and superconducting dome in $TiSe_2$ from electron-phonon interaction. *Arxive*, pp. 1–2, 2011.

[38] van Wezel, J., Nahai-Williamson, P. and Saxena, S.S.: Exciton-photon driven charge density wave in $TiSe_2$. *Physical Review Letters B*, vol. 81, no. 16, pp. 1–8, 2010.

[39] Kassier, G.H.: *Ultrafast Electron Diffraction: Source Development, Diffractometer Design and Pulse Characterisation*. PhD, Stellenbosch University, 2010.

[40] 2010, B.: A brief historical sketch of diffraction theory. Barcelona http://www.cgg.com/technicalDocuments/cggv_0000008612.pdf, Accessed in March 2013.

[41] Rodgers, P.: The double-slit experiment. Physics World http://www.physics.umd.edu/courses/Phys401/appeli/EXTRAS/double-slitexperiment.pdf, Accessed in March 2013.

[42] Ziegler, A.: Ultrafast materials science and 4d imaging with atomic resolution both in space and time. *MRS Bulletin*, vol. 36, no. 11, pp. 121–131, 2011.

[43] Park, H.: *The Development of Femtosecond Electron Diffraction for Direct Measurements of Ultrafast Atomic Motions*. PhD, Florida State University, 2007.

[44] Modla, S.: *Guide to Sectioning on the Reichert-Jung Ultracut E Ultramicrotome*. BioImaging Center Delaware Biotechnology Institute.

[45] Kassier, G.H., Haupt, K., Erasmus, N., Rohwer, E.G., von Bergmann, H.M., Schwoerer, H., Coelho, S.M.M. and Auret, F.D.: A compact streak camera for 150 fs time resolved measurement of bright pulses in ultrafast electron diffraction. *Review of Scientific Instruments*, vol. 81, p. 105103, 2010.

[46] Kittel, C.: *Introduction to Solid State Physics*. John Wiley & sons, Inc., New York, Chichester, 1986.

[47] Lucovsky, G., Liang, W. and White, R.: Reflectivity studies of Ti- and Ta- dichalcogenides: phonons. *Solid State Communications*, vol. 19, pp. 303–307, 1976.

[48] Bayliss, S.C. and Liang, W.Y.: Reflectivity, joint density of states and band structure of group IVb transition-metal dichalcogenides. *J. Phys. C: Solid State Phys.*, vol. 18, pp. 3327–3335, 1985.

[49] Siwick, B.J., Dwyer, J.R., Jordan, R.E. and Miller, R.J.D.: Ultrafast electron optics: Propagation dynamics of femtosecond electron packets. *J. Appl. Phys.*, vol. 92, p. 1643, 2002.

[50] Titov, A.N., Yarmoshenko, Y.M., Zimina, A., Yablonskikh, M.V., Postnikov, A.V. and Eisebitt, S.: Absorption spectroscopic study of the conduction band of titanium dichalcogenides. *Physics of the solid state*, vol. 50, no. 6, pp. 1186–1190, 2008.

[51] Gahlmann, A., Park, S.T. and Zewail, A.H.: Ultrashort electron pulses for diffraction, crystallography and microscopy: Theoretical and experimental resolutions. *Phys. Chem. Chem. Phys.*, vol. 10, p. 2894, 2008.

[52] The imaging source. DMK21BF04 http://www.theimagingsource.com/en_US/products/cameras/firewire-ccd-mono/dmk21bf04/, Accessed in May 2014.

[53] Ashcroft, N.W. and Mermin, N.D.: *Solid State Physics*. Saunders College, Philadelphia, 1976.

[54] van Wezel, J.: Chirality and orbital order in charge density waves. *EPL*, vol. 96, no. 67, pp. 1–5, 2011.

[55] Ishioka, J., Liu, Y.H., Shimatake, K., Kurosawa, T., Ichimura, K., Toda, Y., Oda, M. and Tanda, S.: Chiral charge-density waves. *Physical Review Letters*, vol. 105, no. 17, pp. 1–7, 2010.

[56] van Wezel, J. and Littlewood, P.: Chiral symmetry breaking and charge order. *Physics*, vol. 3, no. 87, pp. 1–3, 2010.